



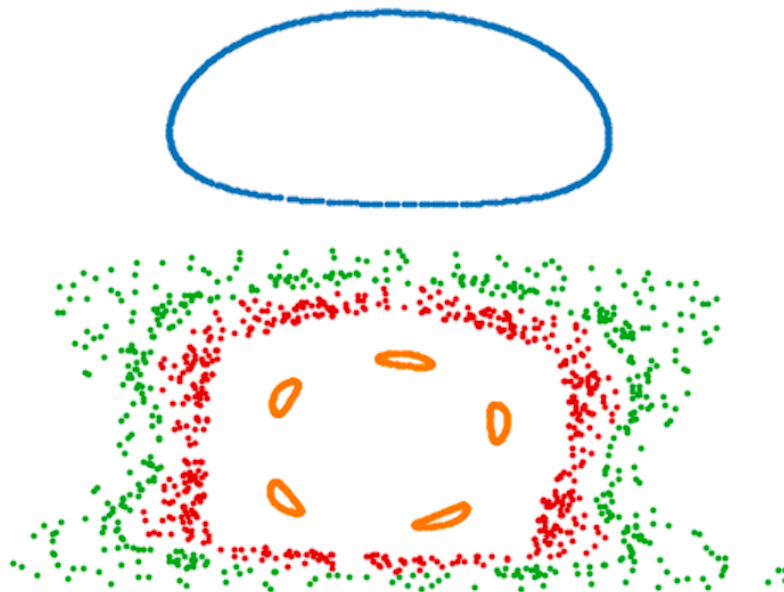
Faculty of Science

# On the occurrence of chaotic advection in a simple model of a tidal flow perturbed by sand waves

BACHELOR THESIS, 15 ECTS

*Jonne Visser, 6154174*

Physics and Astronomy



*Supervisors:*

Prof. dr. H.E. de SWART  
Institute for Marine and Atmospheric Research (IMAU)

Dr. A. NNAFIE  
Institute for Marine and Atmospheric Research (IMAU)

July 14, 2021

## Abstract

The study of passive particle transportation by fluid flow forms an important topic of research, since it can be used to predict trajectories of small particles such as sediment, nutrients and microplastics. What makes this topic even more interesting is that it has been shown by (Aref 1984), (Ottino 1990), (Ridderinkhof and Zimmerman 1992), (Beerens et al. 1994) a.o. that two-dimensional non-integrable Hamilton systems may induce highly irregular trajectories of passive particles. This behaviour is known as stirring by chaotic advection. In this study we use a simple model derived by (Besio et al. 2004) to find an analytical approximation of the flow field of a system with a tidal flow, perturbed by sand waves (shallow tidal area). So far, behaviour of particle trajectories in this system has been studied in two horizontal dimensions by e.g. (Beerens et al. 1994). This study will focus on the system in a vertical plane, in order to assess the influence of particle depth. We use the flow field to numerically calculate the trajectory of passive particles using the symplectic integration method Störmer-Verlet. Through varying the system parameters we find that stirring by chaotic advection occurs in this system for realistic environmental settings. Particles near the surface do not travel significant distances, while particles near the bottom can end up anywhere in the flow. This indicates that tidal currents play a significant role in the transport of particles in shallow tidal areas.

## Contents

<b>1</b>	<b>Introduction</b>	<b>1</b>
<b>2</b>	<b>Model description</b>	<b>4</b>
2.1	Basic state . . . . .	5
2.2	Perturbed state . . . . .	6
2.3	Dimensionless equations . . . . .	6
<b>3</b>	<b>Numerical Method</b>	<b>8</b>
3.1	Symplectic integration method . . . . .	8
3.2	Poincaré sections . . . . .	9
3.3	Fourier spectra . . . . .	10
<b>4</b>	<b>Methodology</b>	<b>12</b>
4.1	Parameters . . . . .	12
4.2	Initial conditions . . . . .	12
4.3	Experiments . . . . .	12
<b>5</b>	<b>Results</b>	<b>15</b>
5.1	Default case - North Sea setting . . . . .	15
5.2	Regions of chaotic stirring . . . . .	17
5.2.1	Varying $\lambda$ . . . . .	17
5.2.2	Varying $\Pi$ . . . . .	21
5.3	Behaviour near chaos . . . . .	22
5.3.1	Varying $\lambda$ . . . . .	22
5.3.2	Varying $\Pi$ . . . . .	26
<b>6</b>	<b>Discussion</b>	<b>30</b>
6.1	Model limitations . . . . .	31
6.2	Future research . . . . .	31
<b>7</b>	<b>Conclusions</b>	<b>32</b>
	<b>Appendices</b>	<b>33</b>
<b>A</b>	<b>Perturbed state velocity field</b>	<b>33</b>
<b>B</b>	<b>Symplectic method</b>	<b>35</b>
B.1	Hamiltonian of the system . . . . .	35
B.2	Splitting methods . . . . .	35
B.3	Non-autonomous systems . . . . .	36
B.4	Component symplectic maps . . . . .	36
B.5	Composition of symplectic maps . . . . .	37
<b>C</b>	<b>Additional results</b>	<b>38</b>
C.1	Regions of chaotic advection - vary $\Pi$ . . . . .	38

## 1 Introduction

The physics of the spreading of particles by fluid flow is an important topic of research. Water currents are responsible for important processes such as distributing nutrients in marine ecosystems and displacing sediment particles on water body bottoms. According to estimates by (Boucher and Friot 2017), one and a half million tons of microplastics are disposed in the ocean every year, and are consequently spread by ocean currents and end up in the food chain. Particles that are very small and have approximately the same density as water, can be approximated by passive particles; passive particles are assumed to always have the same velocity as the fluid. This means that, given an  $n$ -dimensional flow field  $\vec{u}$ , the particle velocity  $\frac{d\vec{x}}{dt}$  is given by

$$\frac{d\vec{x}}{dt} = \vec{u}. \quad (1.1)$$

Study of the trajectories that passive particles take under influence of a fluid flow can help us increase our understanding of the spread and impact of e.g. contaminants, nutrients and sediment, and can help us take appropriate action.

In this study, we will model the behaviour of trajectories of passive particles in shallow tidal areas. Those are areas with a relatively small water depth (in the order of several decameters) with an oscillatory tidal flow with flow speeds in the order of  $O(1\text{m/s})$ . In these areas, tidal forces act on the sediment on the sea floor. If those forces are strong enough, individual sediment grains will be displaced, so that the bottom topography changes over time (Dalrymple and Choi 2003). It turns out that under these circumstances the sediment can form so-called sand waves; oscillatory variations in bottom depth where one wavelength dominates (Besio et al. 2004). This is caused by the inherent feedbacks between the tidal current and the changing bottom topography. These sand waves typically have a wavelength of several hundred meters, and an amplitude of a couple of meters. Figure (1) shows a depth map of the North Sea on the east coast of the Netherlands, illustrating the occurrence sand waves. The bottom figure depicts a cross-section of a sand wave, and illustrates the typical shape of sand waves.

The interactions from the tidal flow with the bottom topography induce a steady perturbed flow. This perturbed flow is periodic with the same period as the sand waves, and circulates in cells with finite horizontal and vertical extent (Campmans 2018). This leads to a very interesting system, where the superposition of the tidal flow with these eddies produces complex behaviour of the trajectories of passive particles; it has been shown by (Aref 1984), (Ottino 1990),

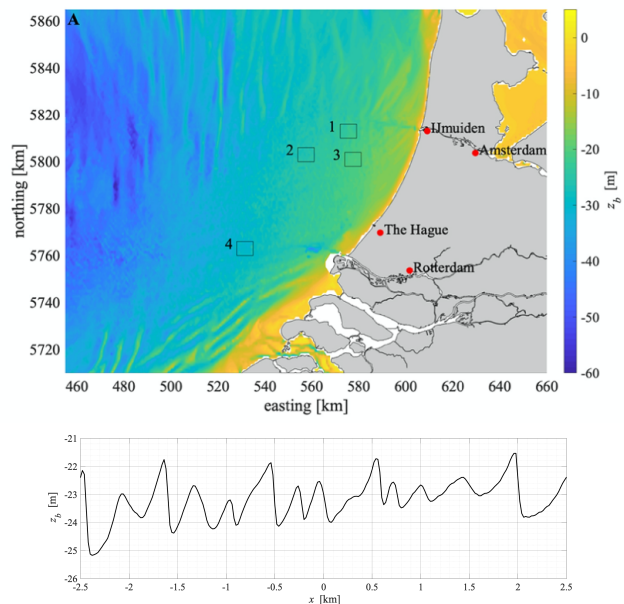


Figure 1: Depth map of the North Sea on the east coast of the Netherlands, together with a cross section of the area marked with a 1 on the map. On the top figure, the horizontal axis points east, the vertical axis points north, and the color indicates the water depth  $z_b$  in meters. In the bottom figure, the horizontal axis points in the direction of the sand waves, and the vertical axis denotes water depth  $z_b$ . Measurement in 2012 by the Hydrografische Dienst van de Koninklijke Marine.

(Ridderinkhof and Zimmerman 1992), (Beerens et al. 1994) a.o. that systems described by a regular two-dimensional Eulerian flow field may induce highly irregular particle trajectories, also known as 'stirring by chaotic advection', or 'Lagrangian chaos'. The trajectories are highly sensitive to slight perturbations, and although deterministic, appear to be random. This chaotic behaviour occurs because the flow can be described by a stream function  $\psi$ , so that the equations governing the particle trajectories obey the Hamilton canonical equations

$$\frac{dx}{dt} = \frac{\partial\psi}{\partial z}, \quad \frac{dz}{dt} = -\frac{\partial\psi}{\partial x}, \quad (1.2)$$

where  $\psi$  acts as Hamiltonian of the system. The amount of chaotic mixing appears to be dependent on two dimensionless parameters, as proposed by Zimmerman 1976. The first relevant parameter  $\lambda$  is defined using two system parameters:  $L$  and  $l$ . Here  $L$  is the tidal excursion length. This is the distance that a passive particle in the tidal current would travel in one period, and  $l$ , the residual eddy diameter, which is the diameter of the circular shape that the residual eddy current makes. We then define  $\lambda$  as  $\lambda = \frac{L}{l}$ . The second relevant parameter  $\nu$  is defined as the ratio of the residual velocity and the tidal velocity.

Where so far mostly particle spreading in shallow tidal areas has been studied in two horizontal dimensions (e.g. Beerens et al. 1994), we will focus on trajectories in a two dimensional plane containing a vertical and a horizontal axis, where the horizontal axis is parallel to the direction of the tidal flow. Vertical analysis is important, because the depth of a particle may be of great importance to its trajectory.

Our analysis of the behaviour of passive particle trajectories will be numerical in nature. Besio et al. 2004 derived an analytical approximation to the velocity field of our system, which they originally used to calculate sediment displacements. We will use this velocity field to study the behaviour of passive particle trajectories on a small scale, spanning several kilometers horizontally and several decameters vertically. The benefit of focussing on a small scale is that we can understand how particles behave in small systems; Sterl et al. 2020 have shown that tidal currents, when viewed on a global scale, can be neglected in studies of the transport of particles in the open ocean. However, their approach yields unreliable results in coastal regions due to uncertainties. This study might supplement their findings to include the qualitative behaviour of particle trajectories in shallow tidal areas.

We will be interested in whether (and when) stirring by chaotic advection occurs. To this end, we will use two parameters similar to Zimmerman's  $\lambda$  and  $\nu$  in order to control our system:

1.  $\lambda$ . This is the ratio of two system parameters. The first is  $L$ , the tidal excursion length. This is the distance that a passive particle in a tidal current would travel in one tidal period. The second system parameter is  $l$ , the wavelength of the sand waves. We calculate  $\lambda$  using  $\lambda = L/l$ . This means that we can see  $\lambda$  as the number of sand waves that a passive particle would travel over in one tidal period.
2.  $\nu$ . This is the height of the sandwaves.

We will see in chapter 2 a motivation for this choice of parameters.

The objectives that we will focus on are to (i): compute the trajectories of passive particles near sand waves for a given environmental setting and describe their behaviour, (ii): Quantify the characteristics of those trajectories and find whether and where stirring by chaotic advection occurs, and (iii): Describe the behaviour of particle trajectories in systems near regions of chaotic advection.

To accomplish this first research goal we will use the Besio et al. 2004 velocity field  $(u(x, z, t), w(x, z, t))$  and the passive particle relations

$$\frac{dx}{dt} = u(x, z, t), \quad \frac{dz}{dt} = w(x, z, t) \quad (1.3)$$

to obtain particle trajectories using a symplectic integration method known as the Störmer-Verlet scheme. This integration method preserves the Hamiltonian structure of the system. We will calculate the specific trajectories for a system with conditions similar to those found in the North Sea. For our second research goal, we will analyse the particle trajectories using Fourier spectra, and we will use the shapes of these spectra as a measure for chaotic advection. Using this, we search for regions where stirring by chaotic advection occurs. For our third research goal, we vary the model parameters starting from systems where chaotic advection occurs.

## 2 Model description

We model our flow in two dimensions; one vertical dimension ( $z$ ), and one horizontal dimension ( $x$ ) parallel to the tidal flow. To model the sand waves, we assume the bottom to be sinusoidal in the  $x$ -direction, aligning the  $z$ -axis so that  $z = 0$  represents the mean bottom height. This means that the bottom height  $\eta(x)$  is given by:

$$\eta(x) = \Pi \cos(kx), \tag{2.1}$$

where  $\Pi$  is the sand wave amplitude and  $k$  is the sand wave wavenumber. We also assume the sea level to be constant at  $z = H$ , also known as the rigid lid assumption. See figure 2 for a sketch of the system.

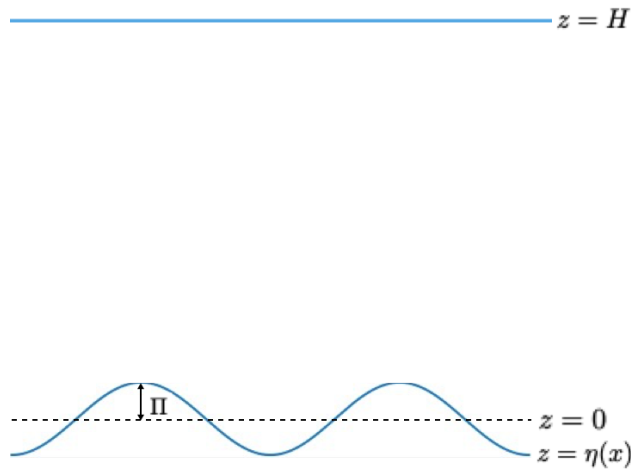


Figure 2: Model sketch of a shallow tidal area with sand waves

In order to model the trajectories of passive particles, we first define the velocity field  $(u, w)$  of the flow; for a fluid parcel at position  $(x, z)$  at time  $t$ , its velocity in the  $x$ -direction is given by  $u(x, z, t)$  and its velocity in the  $z$ -direction is given by  $w(x, z, t)$ . Then what it means for a particle to be passive is that the particle always has the same velocity as the fluid around it, so that the position of a particle  $(x, z)$  is governed by

$$\frac{dx}{dt} = u(x, z, t), \quad \frac{dz}{dt} = w(x, z, t). \tag{2.2}$$

The conservation of mass in our system guarantees that

$$\begin{aligned} & \frac{\partial \rho}{\partial t} + \frac{\partial \rho u}{\partial x} + \frac{\partial \rho w}{\partial z} \\ &= \frac{\partial \rho}{\partial t} + u \frac{\partial \rho}{\partial x} + w \frac{\partial \rho}{\partial z} + \rho \frac{\partial u}{\partial x} + \rho \frac{\partial w}{\partial z} \\ &= \frac{d\rho}{dt} + \rho \frac{\partial u}{\partial x} + \rho \frac{\partial w}{\partial z} \\ &= 0, \end{aligned} \tag{2.3}$$

where  $\rho$  is the fluid density. If we assume the fluid to be incompressible then  $\frac{d\rho}{dt} = 0$ , so that we must have that

$$\frac{\partial u}{\partial x} + \frac{\partial w}{\partial z} = 0. \quad (2.4)$$

Then, according to the fundamental theorem of vector calculus, or Helmholtz's theorem, there must be some function  $\psi(x, z, t)$  such that

$$u(x, z, t) = -\frac{\partial \psi}{\partial z}, \quad w(x, z, t) = \frac{\partial \psi}{\partial x}. \quad (2.5)$$

Note that equations (2.5) are exactly Hamilton's equations, where  $\psi$  acts as a Hamiltonian. This means that equations 2.2 form a Hamiltonian system.

In their paper, Besio et al. 2004 derive an expression for  $\psi$  by performing a linear stability analysis, assuming the bottom perturbations to be small relative to the water depth. This allows them to split the velocity field into two parts. The first part is the basic state  $(u_b, w_b)$ , the velocity field directly caused by tidal forces. The second part is the perturbed state  $(\tilde{u}, \tilde{w})$ , the velocity field caused by the interaction between the tidal flow and the bottom topography (2.1). This means that we can write:

$$u(x, z, t) = u_b(z, t) + \tilde{u}(x, z, t), \quad w(x, z, t) = w_b(z, t) + \tilde{w}(x, z, t).$$

## 2.1 Basic state

The basic state describes the flow field in the absence of bottom waviness. The basic state is calculated by considering the flow over a flat bottom forced by a horizontal pressure gradient, satisfying the Navier-Stokes equations in two dimensions. Together with the continuity equation

$$\frac{\partial u_b}{\partial x} + \frac{\partial w_b}{\partial z} = 0 \quad (2.7)$$

and the fact that the pressure gradient is horizontal so that  $w_b = 0$ , the Navier-Stokes equations reduce to the single momentum equation

$$\frac{\partial u_b}{\partial t} = -\rho^{-1} \frac{\partial p}{\partial x}, \quad (2.8)$$

where  $\frac{\partial p}{\partial x}$  is the horizontal dynamic pressure gradient. The density  $\rho$  is assumed to be constant as well. Besio et al. 2004 used a pressure gradient that is the sum of a steady component and two oscillatory components of angular frequency  $\sigma$  and  $2\sigma$  (where  $\sigma$  is the tidal frequency), which are representative of the residual current, semi-diurnal and quarter-diurnal lunar tidal constituents, respectively. We will use the approach of Gerkema 2000 who only considered the semi-diurnal constituent, so that the tidal flow is driven by the horizontal pressure gradient  $\frac{\partial p}{\partial x} = -\rho P_0 \cos(\sigma t)$ , where  $P_0$  is some constant. Combining with the momentum equation and the boundary conditions

$$u_b = 0 \text{ (at } z = 0 \text{) (no-slip),} \quad \frac{\partial u_b}{\partial z} = 0 \text{ (at } z = H \text{) (rigid-lid),} \quad (2.9)$$

yields an expression for  $u_b$ , which Gerkema 2000 showed can be approximated by

$$u_b(x, z, t) = U_0 z/H(2 - z/H) \cos(\sigma t + \phi),$$

where  $U_0$  is the tidal amplitude and  $\phi$  the tidal phase.



## 2.2 Perturbed state

To model our perturbed state, we use the relations as described by Besio et al. 2004. Just like our total flow, the topologically induced flow is a Hamiltonian system if considered separately; conservation of mass (eq. 2.3) and incompressibility guarantee that there is some function  $\tilde{\psi}(x, z, t)$  such that

$$\tilde{u}(x, z, t) = \frac{\partial \tilde{\psi}}{\partial z}, \quad \tilde{w}(x, z, t) = -\frac{\partial \tilde{\psi}}{\partial x}, \quad (2.11)$$

which are Hamilton's equations where  $\tilde{\psi}$  acts as Hamiltonian. According to Besio et al. 2004 we can describe this function  $\tilde{\psi}$  as

$$\tilde{\psi}(x, z, t) = \Pi \Psi(z, t) e^{ikx} + c.c., \quad (2.12)$$

for some function  $\Psi(z, t)$ . The abbreviation "c.c." means complex conjugate, and it is understood that we add the complex conjugate of the term directly before the '+'-sign. In the paper by Besio et al.,  $\Psi(z, t)$  is split up into its harmonic components  $\Psi_n(z), n \in \mathbb{Z}$ , to represent the effect of each harmonic component of the lunar tide on the perturbed state. This means we can represent  $\Psi$  as

$$\Psi(z, t) = \sum_{n=-\infty}^{\infty} \hat{\Psi}_n(z) e^{in\sigma t}. \quad (2.13)$$

The functions  $\Psi_n(z)$  are to be determined numerically. This means that we can calculate a finite number of harmonic components  $\{\Psi_0(z), \Psi_1(z), \Psi_{-1}(z), \dots, \Psi_N(z), \Psi_{-N}(z)\}$ , for a finite amount of sample points  $\{z_0, \dots, z_M\}$  on the  $z$ -axis.

Combining relations 2.11, 2.12 and 2.13 yields the following velocity field:

$$\tilde{u}(x, z, t) = \Pi \left( \sum_{n=-\infty}^{\infty} \frac{d\hat{\Psi}_n(z, t)}{dz} e^{in\sigma t} e^{ikx} + c.c. \right) \quad (2.14a)$$

$$\tilde{w}(x, z, t) = k\Pi \left( \sum_{n=-\infty}^{\infty} -i\hat{\Psi}_n(z, t) e^{ikx} + c.c. \right). \quad (2.14b)$$

## 2.3 Dimensionless equations

In order to simplify notation, it is beneficial to scale relevant parameters in order to make the governing equations dimensionless. We use the following dimensionless variables (with ' denoting the dimensionless variant):

$$x' = kx \quad z' = \frac{z}{H} \quad t' = \sigma t \quad (2.15a)$$

$$u' = \frac{u}{U_0} \quad w' = \frac{w}{U_0 k H} \quad \Pi' = \frac{\Pi}{H} \quad (2.15b)$$

$$\psi' = \frac{\psi}{U_0 H}. \quad (2.15c)$$

In the dimensionless case, we have that:

$$\frac{\sigma}{k} \frac{dx'}{dt'} = U_0 u', \quad \sigma H \frac{dz'}{dt'} = U_0 k H w', \quad (2.16)$$

so that

$$\frac{dx'}{dt'} = \frac{U_0 k}{\sigma} u', \quad \frac{dz'}{dt'} = \frac{U_0 k}{\sigma} w'. \quad (2.17)$$

Hereafter we shall omit primes, with the understanding that we mean the dimensionless variables.

The dimensionless basic state is given by

$$u_b = \frac{1}{2} z(2 - z) \cos(t). \quad (2.18)$$

As derived in Appendix A, the dimensionless perturbed state is given by

$$\begin{aligned} \tilde{u}(x, z, t) = & 4\Pi \left[ -\frac{1}{2} \frac{d}{dz} \text{Im}(\hat{\Psi}_0(z, t)) \sin(x) \right] \\ & + 4\Pi \sum_{\text{positive odd } n} \left[ \frac{d}{dz} \text{Re}(\hat{\Psi}_n(z, t)) \cos(nt) - \frac{d}{dz} \text{Im}(\hat{\Psi}_n(z, t)) \sin(nt) \right] \cos(x) \\ & + 4\Pi \sum_{\text{positive even } n} \left[ \frac{d}{dz} \text{Re}(\hat{\Psi}_n(z, t)) \sin(nt) - \frac{d}{dz} \text{Im}(\hat{\Psi}_n(z, t)) \cos(nt) \right] \sin(x) \end{aligned} \quad (2.19a)$$

$$\begin{aligned} \tilde{w}(x, z, t) = & -4\Pi \left[ \frac{1}{2} \text{Im}(\hat{\Psi}_0(z, t)) \cos(x) \right] \\ & + 4\Pi \sum_{\text{positive odd } n} \left[ \text{Re}(\hat{\Psi}_n(z, t)) \cos(nt) - \text{Im}(\hat{\Psi}_n(z, t)) \sin(nt) \right] \sin(x) \\ & - 4\Pi \sum_{\text{positive even } n} \left[ \text{Re}(\hat{\Psi}_n(z, t)) \sin(nt) - \text{Im}(\hat{\Psi}_n(z, t)) \cos(nt) \right] \cos(x), \end{aligned} \quad (2.19b)$$

which is the dimensionless form of 2.14a and 2.14b where the complex conjugates have been expanded. We obtain the dimensionless particle velocity using

$$\frac{dx}{dt} = \lambda u_b + \lambda \tilde{u}, \quad \frac{dz}{dt} = \lambda \tilde{w}, \quad (2.20)$$

where  $\lambda = \frac{U_0 k}{\sigma}$ . We see that this definition of  $\lambda$  coincides with the one we gave in the introduction;  $\frac{U_0}{\sigma}$  can be seen as the tidal excursion length, and  $\frac{1}{k}$  is the sand wave wavelength. If we make the dependence on  $\Pi$  explicit by using  $\tilde{u}' = \frac{\tilde{u}}{\Pi}$ ,  $\tilde{w}' = \frac{\tilde{w}}{\Pi}$ , we can rewrite equation (2.20) as

$$\frac{dx}{dt} = \lambda u_b + \lambda \Pi \tilde{u}', \quad \frac{dz}{dt} = \lambda \Pi \tilde{w}', \quad (2.21)$$

making the correspondence between the  $\lambda$  in this system and the  $\lambda$  in the study by Beerens et al. 1994, and the correspondence between  $\Pi$  and the  $\nu$  from Beerens et al. 1994 clear.

### 3 Numerical Method

In order to achieve our first research goal, we will use a numerical integration method to calculate the trajectories of passive particles from the velocity field given in the previous chapter. In order to calculate this velocity field we use a numerical approximation of the functions  $\hat{\Psi}_n$  following the method as outlined in the thesis of Besio et al. 2004. As mentioned before, we need to use a finite number of functions  $\hat{\Psi}_n$ , that are approximated on a finite amount of sample points on the  $z$ -axis. In this study we have chosen to consider the functions  $\hat{\Psi}_0, \hat{\Psi}_1, \hat{\Psi}_{-1}, \hat{\Psi}_2$  and  $\hat{\Psi}_{-2}$  in our calculations. This specific choice of constituents is made because the average value of  $\Psi_n$  decreases rapidly for  $|n| \geq 2$ . We calculate the value of these functions on 201 sample points on the  $z$ -axis, and make a polynomial fit of order 30 to these functions in order to obtain a continuous approximation. With the obtained velocity field we use an integration method to calculate successive positions of particles. The next section of this chapter will be devoted to the symplectic integration method. The section after that will discuss Poincaré sections that are used to efficiently display and analyze particle trajectories. The last section will explain Fourier spectra, with which we will try to achieve our second research goal of quantifying trajectory characteristics.

#### 3.1 Symplectic integration method

Many physical systems have conserved quantities that help analyzing the system. Examples are the famous laws of conservation of mass-energy and momentum. Adopting a numerical method that inherently conserves these quantities may dramatically improve long-time performance and speed. Symplectic integrators aim to conserve the symplectic property of Hamiltonian systems. The symplectic property guarantees the preservation of volume in phase-space (the space of all possible states of the system). More precisely: any Hamiltonian system with canonical coordinates  $\vec{p} = (p_1, \dots, p_n)^T, \vec{q} = (q_1, \dots, q_n)^T$  and Hamiltonian  $H$  obeys

$$\frac{d\vec{p}}{dt} = -\nabla_{\vec{q}}H, \quad (3.1)$$

$$\frac{d\vec{q}}{dt} = \nabla_{\vec{p}}H, \quad (3.2)$$

where  $\nabla_{\vec{q}} = (\frac{d}{dq_1}, \dots, \frac{d}{dq_n})^T$  and  $\nabla_{\vec{p}} = (\frac{d}{dp_1}, \dots, \frac{d}{dp_n})^T$ . From this it follows that

$$\nabla_{\vec{p}} \cdot \frac{d\vec{p}}{dt} + \nabla_{\vec{q}} \cdot \frac{d\vec{q}}{dt} = 0. \quad (3.3)$$

This is also known as Liouville's theorem. This means that if a Hamiltonian system is completely described by a two-dimensional position vector  $\vec{r}$ , then volumes in ordinary space are preserved over time.

The specific symplectic integrator that we will use is the Störmer-Verlet method (Hairer et al. 2006). The method is meant for two-dimensional systems that can be described by canonical coordinates  $p$  and  $q$  and have a Hamiltonian  $H$  of the form

$$H(p, q) = G(p) + F(q), \quad (3.4)$$

for some functions  $G(p)$  and  $F(q)$ .

For some systems it might be possible to perform a coordinate transformation such that the Hamiltonian has this form. In our case there is no such transformation, but we will see in Appendix B

how we can still utilize the Störmer-Verlet method.

Now assume that we have a Hamiltonian  $H$  that can be written as in (3.4). We now have that

$$\frac{dq}{dt} = \frac{dH}{dp} = \frac{dG}{dp}, \quad \frac{dp}{dt} = -\frac{dH}{dq} = -\frac{dF}{dq}. \quad (3.5)$$

Let  $(p(t), q(t))$  denote the state of a particle at time  $t$ . Then we can approximate the state of the particle at time  $t + h$  with the Störmer-Verlet scheme

$$p(t + h) = p(t) - h \frac{dF}{dq}(q_{half}) \quad (3.6a)$$

$$q(t + h) = q_{half} + h \frac{dG}{dp}(p(t + h)), \quad (3.6b)$$

where

$$q_{half} = q(t) + \frac{h}{2} \frac{dG}{dp}(p(t)). \quad (3.7)$$

Although the formal order of the Störmer-Verlet method is only two, Hairer et al. 2003 showed that the order of the error that this method provides scales with step size; the error is of order  $O(h^{\frac{h_0}{h}+1})$ , where  $h_0$  depends on the system. This means that we can obtain results with a much higher accuracy than its formal order suggests.

Since the Störmer-Verlet method requires a very specific form of Hamiltonian, we will have to split the Hamiltonian of our system and perform local time transformations. Appendix B is concerned with the derivation and statement of the method that we will use.

### 3.2 Poincaré sections

The state of a particle in our system is described by three variables; its horizontal and vertical position coordinates  $x$  and  $y$ , and time  $t$ . This means for example that the initial position  $(x(t = 0), z(t = 0))$  fully describes the particle. However, it is difficult to clearly depict the trajectory of a particle in three dimensions. For this reason, we want to condense the particle trajectory into only two dimensions. A useful method for this is the Poincaré section (Tabor 1989); we take a section (two-dimensional subspace) of the phase space, and display precisely this section. Then, while following the trajectories of particles through phase space, we will mark the intersections between these trajectories and the section.

Since we have a three-dimensional phase-space, it suffices to add one constraint to obtain a two-dimensional subspace. Equation (B.3) shows that the system is described by a periodic Hamiltonian with period  $T$ , the period of a tidal cycle. This means that  $H(p, q, t) = H(p, q, t + T)$ . It is therefore natural to consider the section of phase space where  $H(p, q, t) = H(p, q, 0)$ , so that we track the position of the particle precisely every tidal period. A Poincaré section of a system resulting from tidal currents using this particular section is called a Tidal Poincaré section. The resulting family of maps  $T_n$ , that take the initial position of a particle  $(p, q)$  and produce the position of that particle after  $n$  periods is called the tidal map. Figure 3 gives a sketch of a Poincaré section and its tidal map.

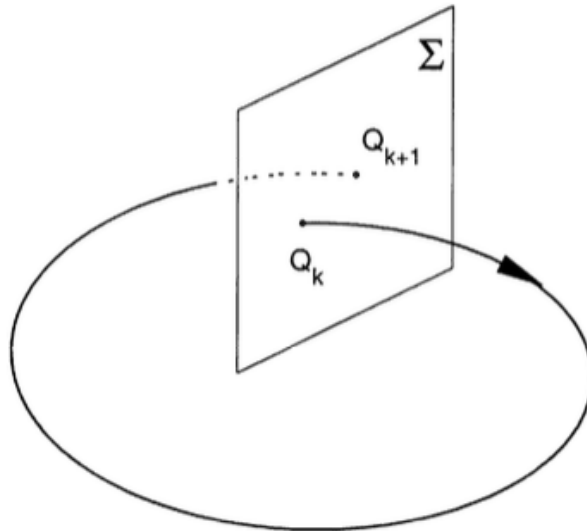


Figure 3: Sketch of Poincaré section ( $\Sigma$ ). Here  $Q_k$  and  $Q_{k+1}$  are intersections between the section  $\Sigma$  and the particle trajectory, and represent successive points on the Poincaré (tidal) map. Image from Abdullaev 1999.

### 3.3 Fourier spectra

Once we have obtained a time series for the trajectory of a particle, we can encode its position vector into a one-dimensional variable. We can do this in many ways, but we want this encoding to preserve nearby points, in the sense that points that are close in space are close in the encoding as well. Functions that obey this property are formally called continuous. We will use the following encoding; given a position vector  $(x, z)$ , its encoding  $E$  is given by:

$$E(x, z) = x + z \quad (3.8)$$

We will take the position of a particle  $(x, z)$  after each tidal period. Then, using the encoding  $E$ , we transform this tidal map into a list of single values. Now the point of Fourier spectra is to identify periodicity in a dataset, using the Fast Fourier Transform (FFT). The FFT can be regarded as a translation of the dataset to frequency space, or a Fourier spectrum (Muller 2015). Periodic datasets will translate to a countable number of 'spikes', whose frequencies share a real common divisor which is the frequency of the original function (see figure (4)). One may identify quasi-periodicity if the Fourier spectrum has a finite amount of spikes, but if they do not share a real common divisor (for example, if the Fourier spectrum has two spikes, one at a rational frequency and one at an irrational frequency). Although continuity of the Fourier spectrum does not directly guarantee chaotic behaviour, it does seem to be a good indicator in our system. We will therefore quantify chaos by the width of the continuous non-zero sections in a Fourier spectrum (see figure (5b)). We will call this width the noise width. The frequencies in Fourier spectra of tidal maps are easily expressed in terms of  $\sigma$ , the tidal frequency. To ease notation, we will scale noise widths with  $\sigma$ , so that we obtain a dimensionless parameter that denotes noise width. In the rest of this study we will write noise width in dimensionless form.

Note that, with a finite amount of data points, it is impossible to identify continuous regions with certainty. Spikes however will have a very small noise width, so that Fourier spectra of non-chaotic particle trajectories will naturally have a small noise width. More specifically, we will define that

particle trajectories whose Fourier spectra have noise widths larger than or equal to 0.04 are chaotic. This value follows from experimentation.

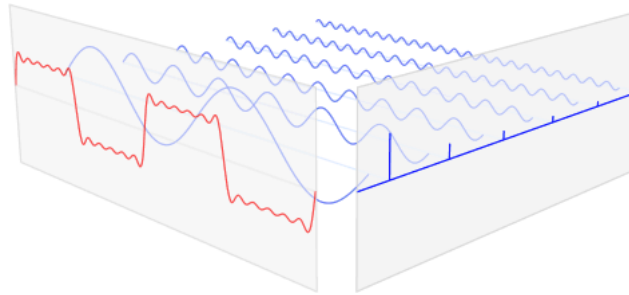
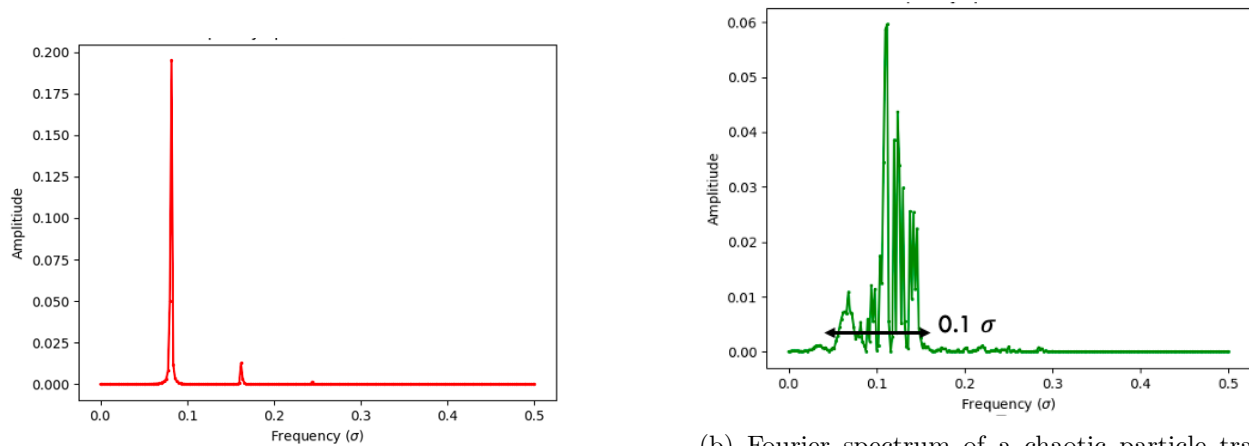


Figure 4: Fourier transformation of a periodic function. The red graph represents the original function, and the blue graph represents the Fourier spectrum. The sinusoidal wave functions in between represent the frequency components of the original function.



(a) Fourier spectrum of a non-chaotic particle trajectory. Non-chaotic trajectories result in Fourier spectra with small spikes.

(b) Fourier spectrum of a chaotic particle trajectory. The width of the non-zero 'continuous' section is indicated by the arrow, and is called the noise width. A bigger noise width indicates more chaotic advection.

Figure 5: Fourier spectra of a periodic and a chaotic particle trajectory. The horizontal axis shows the frequency, scaled by the tidal frequency of the semi-diurnal (M2) constituent, and the vertical axis denotes frequency amplitude.

## 4 Methodology

### 4.1 Parameters

The numerical methods introduced in the previous chapter require the choice of numerical parameters. The step size is important, because a smaller step size increases the accuracy of the calculation. A smaller step size also means that the computation costs more time. The step size is chosen to be  $h = \frac{2\pi}{N}$ , where  $N = 1000$ . This means that the particle position is calculated 1000 times per tidal period. This value follows from experience.

In 2.19a and 2.19b we can see that, theoretically, there is an infinite number of functions  $\hat{\Psi}_n$  that we can consider. However, since this is impossible in a numerical method, we have to truncate after some amount of harmonic components  $\hat{\Psi}_n$ . Since the relative contribution of functions  $\hat{\Psi}_n$  seems to decline rapidly after  $n = 2$ , we use only the first three harmonic components;  $\hat{\Psi}_0$ ,  $\{\hat{\Psi}_1, \hat{\Psi}_{-1}\}$  and  $\{\hat{\Psi}_2, \hat{\Psi}_{-2}\}$ . Note that we bundle the functions  $\hat{\Psi}_n$  and  $\hat{\Psi}_{-n}$  together, because we can extract the value of one from the other using the relation that  $\hat{\Psi}_{-n}^* = \hat{\Psi}_n$  if  $n$  is odd, and  $\hat{\Psi}_{-n}^* = -\hat{\Psi}_n$  if  $n$  is even. For the discretization of the functions  $\hat{\Psi}_n$  we use 201 points in the  $z$ -direction, for which we sample their value using the method in Besio et al. 2004. In figure 6 we see the discrete approximations of the three harmonic components and their fits, as described in the previous chapter.

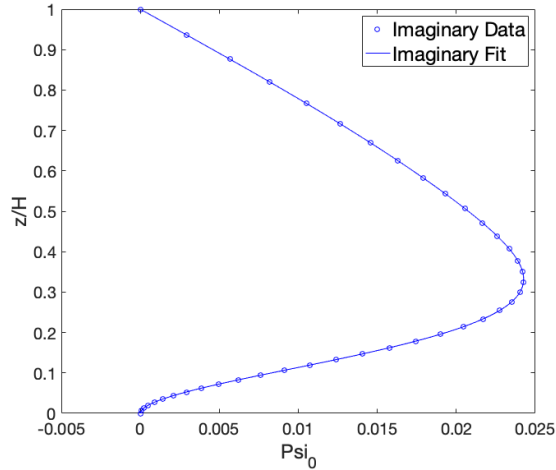
### 4.2 Initial conditions

In all experiments we will use the same initial conditions, with  $x$ -coordinate  $2.5kx/\pi$ , and  $z$ -coordinates  $\{0.34, 0.42, 0.5, 0.57\} \frac{1}{H}$ . We have only one  $x$ -coordinate because exploratory experiments have shown that particles starting on the line where  $xk/\pi = 2.5$  show the same qualitative trajectories as those not starting on that line. We use these specific  $z$ -coordinates because exploratory experiments have shown  $z/H = 0.5$  to be a line around which interesting stuff happens, so we want to explore close to that line. The coordinates are biased towards the lower end because regions where  $z/H < 0.5$  shows the most potential to be regions of chaotic advection. In all experiments we will model over 500 tidal periods.

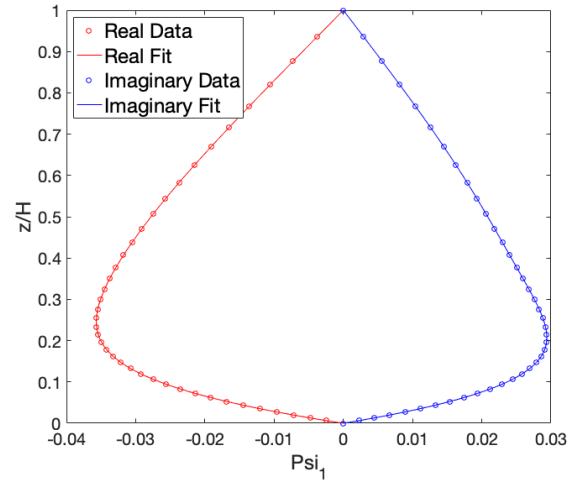
### 4.3 Experiments

In order to achieve our first research goal, we choose the North Sea as our environmental setting. We will look at the typical parameter values in this setting. For  $H$ , the water depth, we choose  $H = 23$  m. Although the grain size of the sand on the bottom varies, we assume that the sand grains only have one size  $r_s = 0.275$  mm. The amplitude of the M2 current is 0.65 m/s. The oscillation frequency of the M2 current  $\sigma$  is  $1.4 \cdot 10^{-4}$  rad/s. Using these parameters, the typical sand wave wavelength is 457.9 m. This means that we have that  $\lambda = \frac{U_0 k}{\sigma}$  is around 15. The typical sand wave height is around  $2m$ , so that  $\Pi = \frac{2}{H} \approx 0.1$ . Our first experiment "Default" will use these parameter values to calculate the behaviour of particle trajectories under these circumstances.

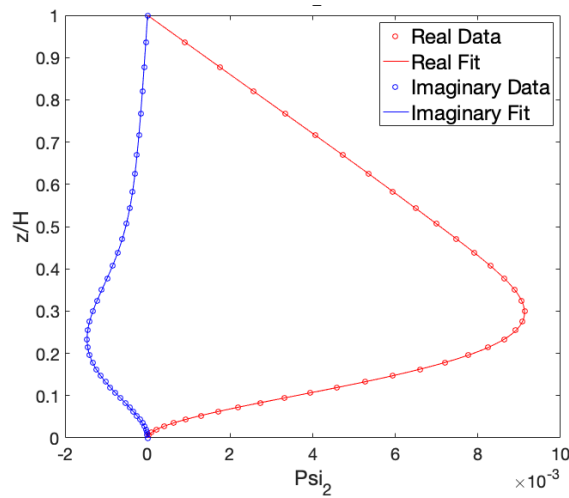
In order to achieve our second research goal of finding regions where chaotic stirring by advection occurs, we will perturb  $\lambda$  and  $\Pi$  from these default values to see where chaotic advection occurs. More specifically, we will do two experiments: "SearchVar- $\lambda$ ", where we vary  $\lambda$  between 8 and 15 in eight steps while keeping  $\Pi = 0.1$ , and the experiment "SearchVar- $\Pi$ ", where we will vary  $\Pi$  between 0.05 and 0.12 in 8 steps, while keeping  $\lambda = 15$ . We have chosen these values because initial experiments have shown that particles in systems with parameters in these ranges exhibit interesting behaviour. In both experiments we will keep track of the noise width of the Fourier spectrum of particle trajectories.



(a) Data and polynomial fit to  $\Psi_0$ . The mean square error between the fit and the data is  $4.9956 \cdot 10^{-29}$ .



(b) Data and polynomial fit to  $\Psi_1$ . The mean square error between the fit and the data of the real part is  $1.2858 \cdot 10^{-28}$ . The mean square error between the fit and the data of the imaginary part is  $1.1667 \cdot 10^{-28}$ .



(c) Data and polynomial fit to  $\Psi_2$ . The mean square error between the fit and the data of the real part is  $1.0830 \cdot 10^{-29}$ . The mean square error between the fit and the data of the imaginary part is  $3.3335 \cdot 10^{-31}$ .

Figure 6: Real and imaginary parts of the harmonic constituents  $\Psi_0$ ,  $\Psi_1$  and  $\Psi_2$  considered in the model. The dots represent the numerical approximation following the model by Besio et al. The lines represent the polynomial fit.

For our third research goal we will take a region where we found stirring by chaotic advection, and perturb  $\lambda$  and  $\Pi$  from there in small steps. More specifically, we will investigate the behaviour of particle trajectories close to the region  $\lambda = 10.14, \Pi = 0.1$ , where we will see occurs stirring by chaotic advection. We will do this in two experiments: "ZoomVar- $\lambda$ ", where we vary  $\lambda$  between 9 and 11.5 in 20 steps, while keeping  $\Pi = 0.1$ . The second experiment is "ZoomVar- $\Pi$ ", where we vary  $\Pi$  between 0.05 and 0.12 in 10 steps, while keeping  $\lambda = 10.14$ .



---

	$\lambda$	$\Pi$	steps
<b>Default</b>	15	0.1	1
<b>SearchVar-<math>\lambda</math></b>	8 – 15	0.1	8
<b>SearchVar-<math>\Pi</math></b>	15	0.05 – 1.12	8
<b>ZoomVar-<math>\lambda</math></b>	9 – 11.5	0.1	20
<b>ZoomVar-<math>\Pi</math></b>	10.14	0.05 – 0.12	10

## 5 Results

### 5.1 Default case - North Sea setting

The tidal map for the default case described in section 4.3, representing a North Sea setting, is shown in Figure (8), with close-ups of the areas where  $2.0 \leq kx/\pi \leq 3.0$  and  $0.0 \leq kx/\pi \leq 1.0$  in Figure (9). The flow field of the perturbed state (so the flow field without the unperturbed tidal current) in this case at  $t = 0$  is depicted in Figure (7). In this figure we see that the perturbed flow circulates in cells. Those cells span between adjacent troughs and crests in the sand waves. We can identify two different kinds of cells; those where  $0 \leq z/H \leq 0.35$ , and those where  $0.35 \leq z/H \leq 1$ . The magnitude of the velocities in the cells near the bottom are about three times higher than those in the cells near the surface.

Figures (8) and (9) show a significant qualitative difference in the behaviour of particle trajectories between particles where  $z/H > \sim 0.5$  and those where  $z/H < \sim 0.5$ . It is therefore convenient to treat those cases separately.

Tidal maps of particles where  $z/H > \sim 0.5$  (more precisely, the particles above the black curved lines in Figure (9)) trace semi-circle-like trajectories around an elliptical point at  $z/H = 0.6$ ,  $kx/\pi = (m + 0.5)$  for some  $m \in \mathbb{Z}$ . Trajectories further from this elliptical point become more spread-out; the blue trajectory in figure (9a) is close to the elliptical point (furthest vertical separation  $\sim 0.05z/H$ ), and its tidal map traces a thin line. The green trajectory in (9a) has a furthest vertical distance to its elliptical point of  $\sim 0.25z/H$ , and has a confetti-like semi-circle structure with maximal vertical width  $\sim 0.05z/H$ . The red trajectory in figure (9b) has a furthest vertical separation to its elliptical point of  $\sim 0.35z/H$ , and has a confetti-like semi-circle structure with maximal vertical width  $\sim 0.15z/H$ .

Tidal maps of particles where  $z/H < \sim 0.5$  or below the black curved lines in Figure (9) are more cloud-like, not adhering to any elliptical points. We see in figure (8) that the red and orange trajectories move freely over the span of three sand wave wavelengths. We can see in both figures (9a) and (9b) that the orange tidal map is more dense around points where  $z/H = 0.2$  or  $z/H = 0.35$ , while  $kx/\pi = (m + 0.5)$  for some  $m \in \mathbb{Z}$ . We can also see that the red tidal map, while first moving freely between cells below  $z/H \sim 0.5$ , moves above  $z/H \sim .5$  and gets caught around an elliptical point at  $z/H = 0.6$ ,  $kx/\pi = 0.5$ . So, while the red particle has an initial position between the trough and crest at  $z/H = 2$  and  $z/H = 3$ , it ends up getting trapped above a different sand wave. Looking at the Fourier-spectra of the trajectories, we see that the spectrum of the blue trajectory has a noise width of about  $0.01\sigma$ . The spectrum of the orange trajectory has a noise width of about  $0.025\sigma$ . The spectrum of the green trajectory has a noise width of about  $0.06\sigma$ , and the spectrum of the red trajectory has a noise width of about  $0.04\sigma$ .

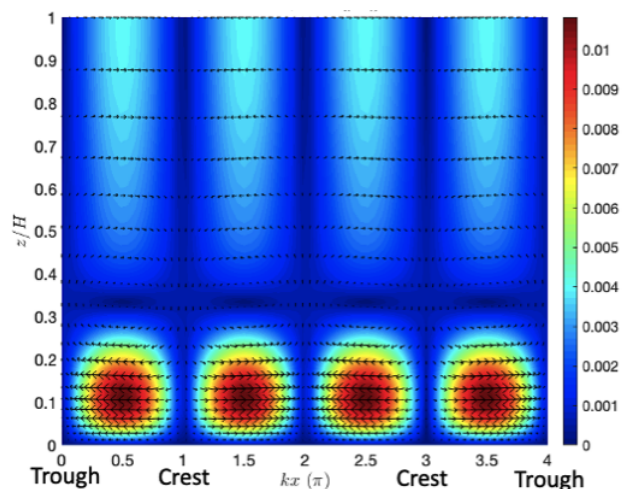


Figure 7: Flow field of the perturbed state in the default case at  $t = 0$ . The arrows represent the direction of the flow, and the color represents the (dimensionless) magnitude of the flow.

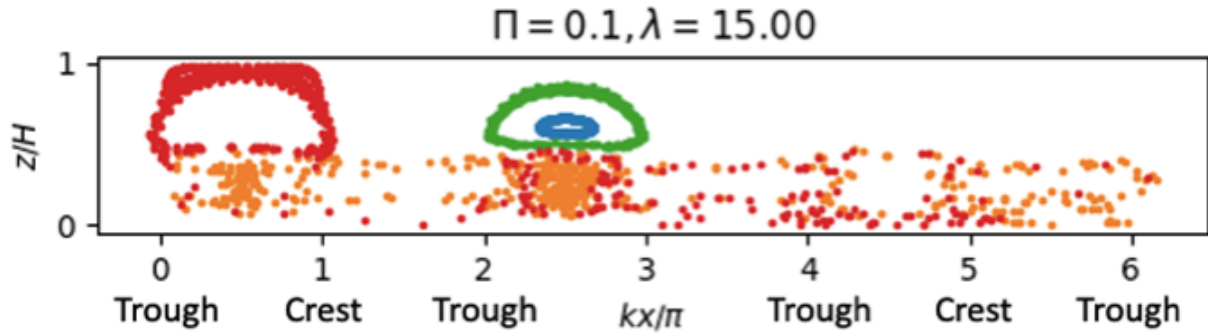
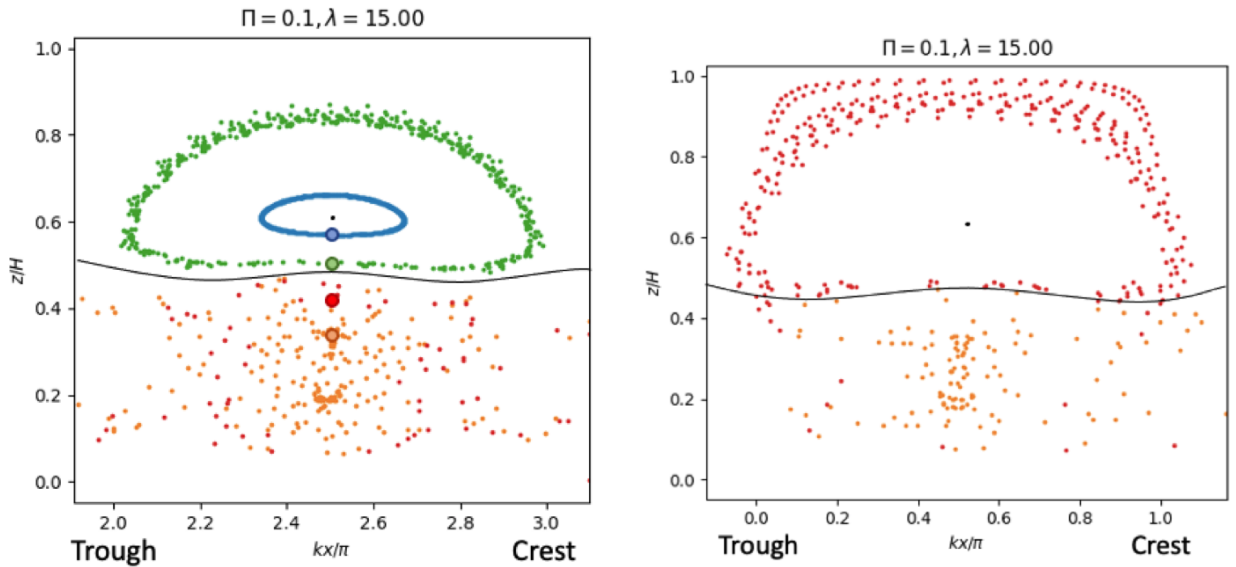


Figure 8: Tidal map representing the default environmental setting representing the North Sea, using  $\Pi = 0.1$  and  $\lambda = 15.00$ . For  $z/H > 0.5$ , trajectories revolve around an elliptic point at  $kx/\pi = (m + 0.5), m \in \mathbb{Z}, z/H = 0.6$ . For  $z/H < 0.5$ , trajectories show a confetti-like structure, and travel between cells. The red trajectory starts traveling between cells, but ends up revolving around an elliptic point at  $kx/\pi = 0.5$ .



(a) Close-up of the tidal map for  $2.0 \leq kx/\pi \leq 3.0$ . The figure shows that trajectories become less confetti-like if they come closer to the elliptic point at  $kx/\pi = 2.5, z/H = 0.6$ . The orange tidal map forms clumps at  $kx/\pi = 2.5, z/H = 0.2$  and  $z/H = 0.35$ . The colored circles denote the initial positions of the particles with corresponding color.

(b) Close-up of the tidal map for  $0.0 \leq kx/\pi \leq 1.0$ . The figure again shows the clumps at  $z/H = 0.2$  and  $z/H = 0.35$  in the tidal map of the orange particle. The red particle starts orbiting around an elliptic point at  $kx/\pi = 0.5, z/H = 0.6$ , and keeps its confetti-like structure.

Figure 9: Close-ups of figure 8. The black line denotes the imaginary line below which particles travel between the sand waves.

## 5.2 Regions of chaotic stirring

As we saw in the previous section, we have already found a region of chaotic advection for the default case. In this series of experiments we will try to find other regions of chaotic advection.

### 5.2.1 Varying $\lambda$

The tidal maps from experiment "SearchVar- $\lambda$ " are shown in figures (11) and (12). In the figures, we see seven different trajectories for constant  $\Pi = 0.1$  and  $\lambda$  varying between 8 and 14.43. Note that the  $z$ -axis is not always on the same scale. This is because the particles orbit different elliptic points for different values of  $\Pi$  and  $\lambda$ . This means that the maps sometimes only span a part of the  $z$ -axis. In order to obtain detailed figures, the  $z$ -axes are scaled accordingly.

Figure (11a) shows the tidal maps for  $\Pi = 0.1$  and  $\lambda = 8.00$ . The maps of the red, green and blue trajectories orbit around an elliptic point at  $z/H = 0.65$ ,  $kx/\pi = 2.5$ , and the map of the orange trajectory orbits around an elliptical point at  $z/H = 0.15$ ,  $kx/\pi = 2.5$ . The Fourier spectra of the red, green and blue trajectories have a noise width of about 0.01, and the Fourier spectrum of the orange trajectory has a noise width of about 0.03. This means that there is no chaotic stirring for these parameter values.

Figure (11b) shows the tidal map for  $\Pi = 0.1$  and  $\lambda = 9.07$ . This time the maps orbit around a single elliptic point at  $z/H = 0.38$ ,  $kx/\pi = 2.5$ . Their Fourier spectra all have a noise width of about 0.01, so we do not find a region of chaotic stirring here.

Figure (11c) shows the tidal map for  $\Pi = 0.1$  and  $\lambda = 10.14$ . The map of the blue trajectory orbits around an elliptical point at  $z/H = 0.7$ ,  $kx/\pi = 2.5$ , and the maps of the green, red and orange trajectories orbit around an elliptical point at  $z/H = 0.25$ ,  $kx/\pi = 2.5$ . The blue trajectory traces a smooth line, while the tidal map of the red and green trajectories gives a confetti-like structure. The orange trajectory jumps between five 'islands'. The Fourier spectra of the blue and orange trajectories have a noise width of about 0.01, that of the green trajectory has a noise width of about 0.13, and that of the red trajectory of about 0.04. This means that, looking at the figure, we find a region of chaotic stirring for  $z/H < 0.5$ . The amount of chaotic stirring is determined by the distance of the particle to the elliptic point at  $z/H = 0.25$ ,  $kx/\pi = 2.5$ .

Figure (11d) shows the tidal map for  $\Pi = 0.1$  and  $\lambda = 11.21$ . The maps of the trajectories orbit around an elliptical point at  $z/H = 0.45$ ,  $kx/\pi = 2.5$ , and their Fourier spectra have a noise width of about 0.01. This means that the region of chaotic stirring from the previous figure has disappeared.

Figure (12a) shows the tidal map for  $\Pi = 0.1$  and  $\lambda = 12.00$ . The map of the blue trajectory orbits around an elliptical point at  $z/H = 0.75$ ,  $kx/\pi = 2.5$ , and the maps of the green, red and orange trajectories orbit around an elliptical point at  $z/H = 0.3$ ,  $kx/\pi = 2.5$ . The Fourier spectra of the blue, red and orange trajectories have a noise width of about 0.01, while the Fourier spectrum of the green trajectory has a noise width of about 0.1. This means that these parameter values give rise to a region of chaotic stirring for particles where  $z/H < \sim 0.55$  far enough from the elliptic point at  $z/H = 0.3$ ,  $kx/\pi = 2.5$ .

Figure (12b) shows the tidal map for  $\Pi = 0.1$  and  $\lambda = 13.36$ . The maps of the trajectories orbit around an elliptical point at  $z/H = 0.48$ ,  $kx/\pi = 2.5$ , where the blue maps form six islands around the elliptic point. The Fourier spectra of the blue, red and green trajectories have a noise width of about 0.01, while the Fourier spectrum of the orange trajectory has a noise width of about 0.03.

Figure (12c) shows the tidal map for  $\Pi = 0.1$  and  $\lambda = 14.43$ . In this case we see that the tidal maps of the red, green and orange trajectories orbit an elliptic point at  $z/H = 0.3$ ,  $kx/\pi = 2.5$ , while the map of the blue trajectory shows a confetti-like structure, and does not adhere to an elliptic point. Although the trajectory of the blue particle seems chaotic, the noise width of its Fourier spectrum is only 0.02. The noise width of the red, green and orange Fourier spectra are about 0.01. This means that we do not identify any chaotic advection for these parameter values.

Figure (10) shows the maximum noise width as a function of  $\lambda$  for constant  $\Pi = 0.1$ . The line at noise width 0.04 denotes the line above which we consider the particle trajectory to be chaotic. We see that we can identify two regions of stirring by chaotic advection; around  $\lambda = 10.14$ ,  $\Pi = 0.1$  and around  $\lambda = 12$ ,  $\Pi = 0.1$ . These regions appear to be singular, in the sense that there does not seem to be a larger trend where, for example, the noise width increases with  $\lambda$ .

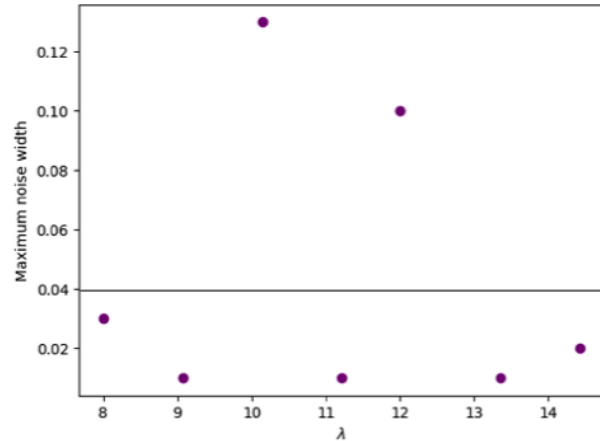


Figure 10: Maximum noise width (vertical axis) as a function of  $\lambda$  (horizontal axis). The black horizontal line at noise width 0.04 denotes the noise width above which trajectories are considered chaotic.

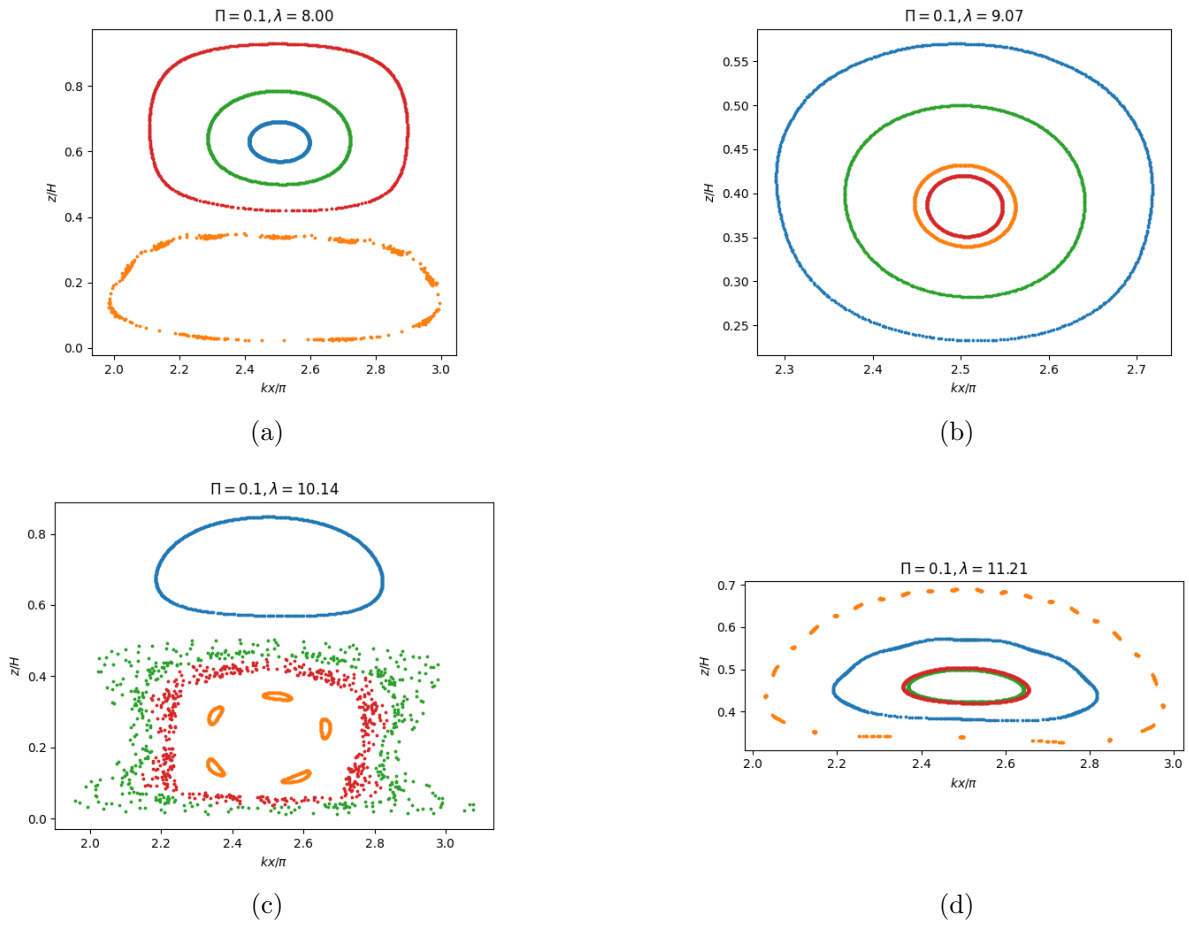


Figure 11: Tidal maps for constant  $\Pi = 0.1$ , and for varying  $\lambda$  between 8 and 11.21.

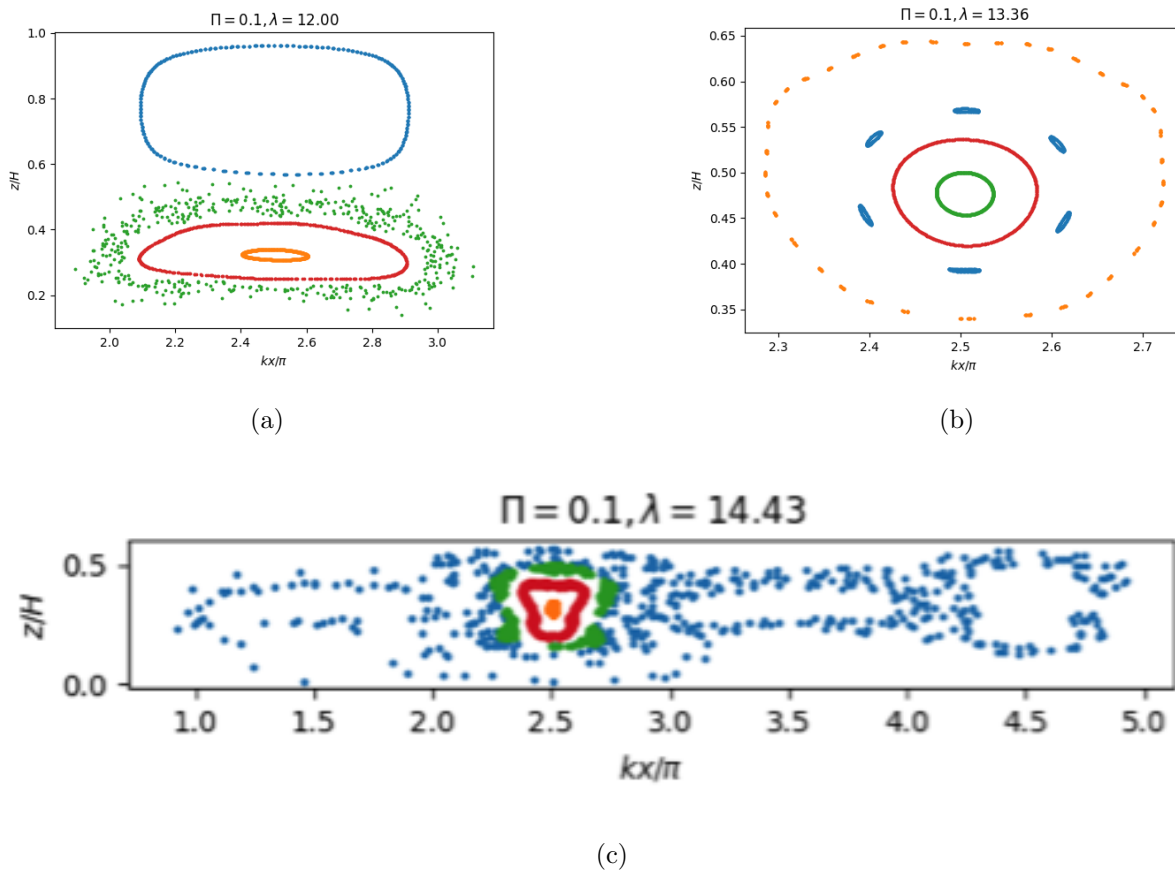


Figure 12: Tidal maps for constant  $\Pi = 0.1$ , and for varying  $\lambda$  between 12 and 14.43.

### 5.2.2 Varying $\Pi$

In the experiment "SearchVar- $\Pi$ ", we vary  $\Pi$  between 0.05 and 0.13 in six steps while keeping  $\lambda = 15$ . The results for varying  $\Pi$  are comparable to those above when varying  $\lambda$ . Therefore the figures will not be displayed in the main text. An interested reader may take a look at the figures in appendix C, section (C.1).

Figure (13) shows the maximum found noise width as a function of  $\Pi$ . The black line at a noise width value of 0.04 shows the line above which trajectories are considered chaotic. We see a general trend that the maximal noise width increases as  $\lambda$  increases. We also observe a spike in noise width at  $\Pi = 0.067$ . We can therefore say that there are regions of chaotic stirring at  $\Pi = 0.067, \lambda = 15$  and at  $\Pi \geq 0.08, \lambda = 15$ .

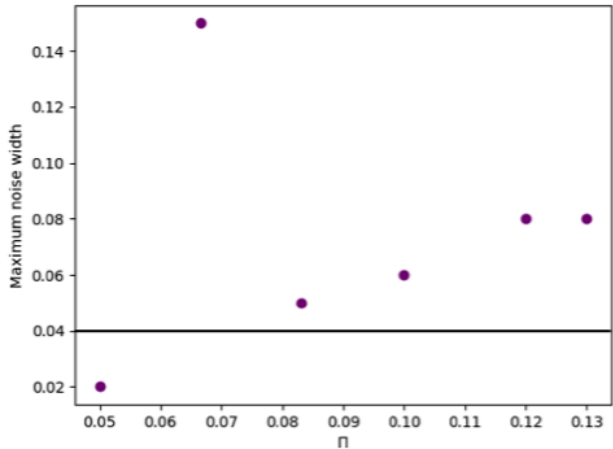


Figure 13: Maximum noise width (vertical axis) as a function of  $\Pi$  (horizontal axis). The black horizontal line at noise width 0.04 denotes the noise width above which trajectories are considered chaotic.



### 5.3 Behaviour near chaos

In the next set of experiments we will assess the sensitivity of the system on the parameters  $\lambda$  and  $\Pi$  near a found region of chaotic advection; in particular we will vary  $\lambda$  and  $\Pi$  around  $\lambda = 10.14$ ,  $\Pi = 0.1$ .

#### 5.3.1 Varying $\lambda$

The tidal maps from experiment "ZoomVar- $\lambda$ " are shown in figures (15) and (16). In the figures, we see eight different trajectories for constant  $\Pi = 0.1$  and  $\lambda$  varying between 9 and 11.25.

Figure (15a) shows the tidal map for  $\Pi = 0.1$  and  $\lambda = 9.19$ . The maps of the trajectories orbit around an elliptical point at  $z/H = 0.35$ ,  $kx/\pi = 2.5$ , and trace a dotted line. The Fourier spectra of all trajectories have noise widths of about 0.01.

Figure (15b) shows the tidal map for  $\Pi = 0.1$  and  $\lambda = 9.38$ . The particles orbit around the same elliptic point. The maps of the red and orange trajectories trace a continuous looking line, while the maps of the green and blue trajectories have big gaps. The Fourier spectra of all trajectories have noise widths of about 0.01.

Figure (15c) shows the tidal map for  $\Pi = 0.1$  and  $\lambda = 9.56$ . The particles orbit around an elliptical point that is a bit closer to the bottom, at  $z/H = 0.3$ . The maps of the red and orange trajectories trace a continuous looking line, while the points in the tidal map of the green particle have grown to eight islands. The map of the blue trajectory looks a bit erratic and has many small gaps. The Fourier spectra of all trajectories have noise widths of about 0.01.

Figure (15d) shows the tidal map for  $\Pi = 0.1$  and  $\lambda = 9.75$ . Here we see that the orange, red and green particles orbit around the same elliptic point, but the blue particle now starts traveling between two sand waves, showing a confetti-like structure. While the noise width of the Fourier spectra of the orange, red and green particles are around 0.01, the noise width of the Fourier spectrum of the blue particle is around 0.05, meaning that the blue particle is in a region of chaotic stirring.

Figure (15e) shows the tidal map for  $\Pi = 0.1$  and  $\lambda = 9.94$ . We now see that the particles orbit around two elliptic points. The map of the blue trajectory traces a continuous looking line, and orbits around an elliptical point at  $z/H = 0.7$ ,  $kx/\pi = 2.5$ . Its Fourier spectrum has a noise width of about 0.02. The maps of the green, red and orange trajectories orbit around an elliptical point at  $z/H = 0.25$ ,  $kx/\pi = 2.5$ . The map of the red trajectory traces a continuous looking line, while the map of the orange trajectory jumps between five islands. The map of the green trajectory has a confetti-like structure. The Fourier spectrum of the orange and red orbits have a noise width of about 0.01, that of green has a noise width of about 0.08. This means that the region of chaotic stirring is now stronger than in the previous figure.

Figure (16a) shows the tidal map for  $\Pi = 0.1$  and  $\lambda = 10.12$ . The map of the blue trajectory traces a continuous looking line, and orbits around an elliptical point at  $z/H = 0.7$ ,  $kx/\pi = 2.5$ . Its Fourier spectrum has a noise width of about 0.01. The maps of the red and orange trajectories orbit around an elliptical point at  $z/H = 0.25$ ,  $kx/\pi = 2.5$ . The map of the orange trajectory jumps between five islands, and the map of the red and green trajectories have a confetti-like structure. Furthermore, the map of the green particle jumps between two different sand waves. The Fourier spectrum of the orange orbit has a noise width of about 0.01, that of green has a noise width of about 0.08, and that of the red trajectory has a noise width of about 0.05. We see that the region of chaotic stirring has not increased in strength, but in width; now two of our particles are in this region.

Figure (16b) shows the tidal map for  $\Pi = 0.1$  and  $\lambda = 10.50$ . The map of the blue and green trajec-

tory trace a continuous looking line, and orbit around an elliptical point at  $z/H = 0.6$ ,  $kx/\pi = 2.5$ . Their Fourier spectrum has a noise width of about 0.01. The map of the orange trajectory orbits around an elliptical point at  $z/H = 0.25$ ,  $kx/\pi = 2.5$ , and jumps between five islands. The map of the red trajectory has a confetti-like structure, and jumps between three different sand waves. The Fourier spectrum of the orange and green orbit has a noise width of about 0.01, and that of the red trajectory has a noise width of about 0.03. We see that the region of chaotic advection has disappeared.

Figure (16c) shows the tidal map for  $\Pi = 0.1$  and  $\lambda = 10.69$ . The maps of the red, green and blue trajectories trace a continuous looking line, and orbit around an elliptical point at  $z/H = 0.55$ ,  $kx/\pi = 2.5$ . The Fourier spectrum of the green and blue trajectories has a noise width of about 0.01, and that of the red trajectory has a noise width of about 0.02. The map of the orange trajectory has a confetti-like structure, and jumps between the trough and crest of a sand wave. The Fourier spectrum of the orange orbit has a noise width of about 0.17. This is a sudden spike in noise width, that indicates that the orange particle is in a region of chaotic advection.

Figure (16d) shows the tidal map for  $\Pi = 0.1$  and  $\lambda = 11.25$ . The maps of the trajectories orbit around an elliptical point at  $z/H = 0.45$ ,  $kx/\pi = 2.5$ . The maps of the red and green trajectories trace a continuous looking line, and their Fourier spectrum has a noise width of about 0.01. The map of the blue trajectory also has some small gaps, and its Fourier spectrum has a noise width of about 0.01. The orange trajectory has a confetti-like structure, and its Fourier spectrum has a noise width of about 0.03. There is no chaotic advection in the system anymore.

We can see in figures (16a), (16b) and (16c) that tidal maps may switch sand wave cells (integer values on the  $kx/\pi$ -axis) if they are in mixing regions. Although the trajectories in figure (16d) are far less chaotic than in the figures before it, there are no islands in this figure. This might indicate that the bifurcation of elliptic points does not work in every direction.

Figure (14) shows the maximum noise width as a function of  $\lambda$ . The black line again denotes the threshold above which we consider there to be a region of chaotic stirring. We see that the maximum noise width increases between  $\lambda = 9.6$  and  $\lambda = 10.2$ , after which the noise width rapidly decreases, increases and then decreases again. This means that, approaching a region of chaotic stirring from lower values of  $\lambda$ , the strength of the region of chaotic advection steadily increases, while increasing  $\lambda$  after that means that regions of chaotic advection change rapidly.

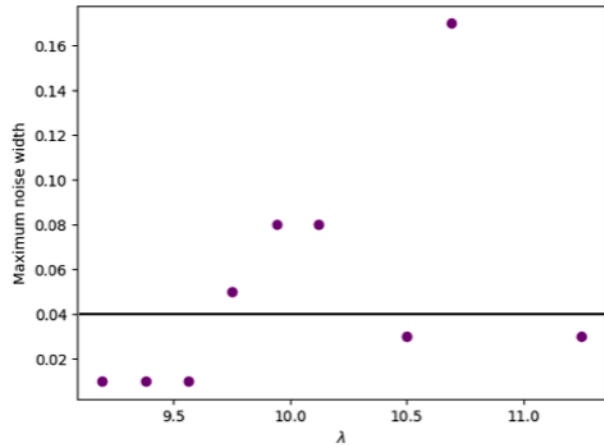


Figure 14: Maximum noise width (vertical axis) as a function of  $\lambda$  (horizontal axis). The black horizontal line at noise width 0.04 denotes the noise width above which trajectories are considered chaotic.

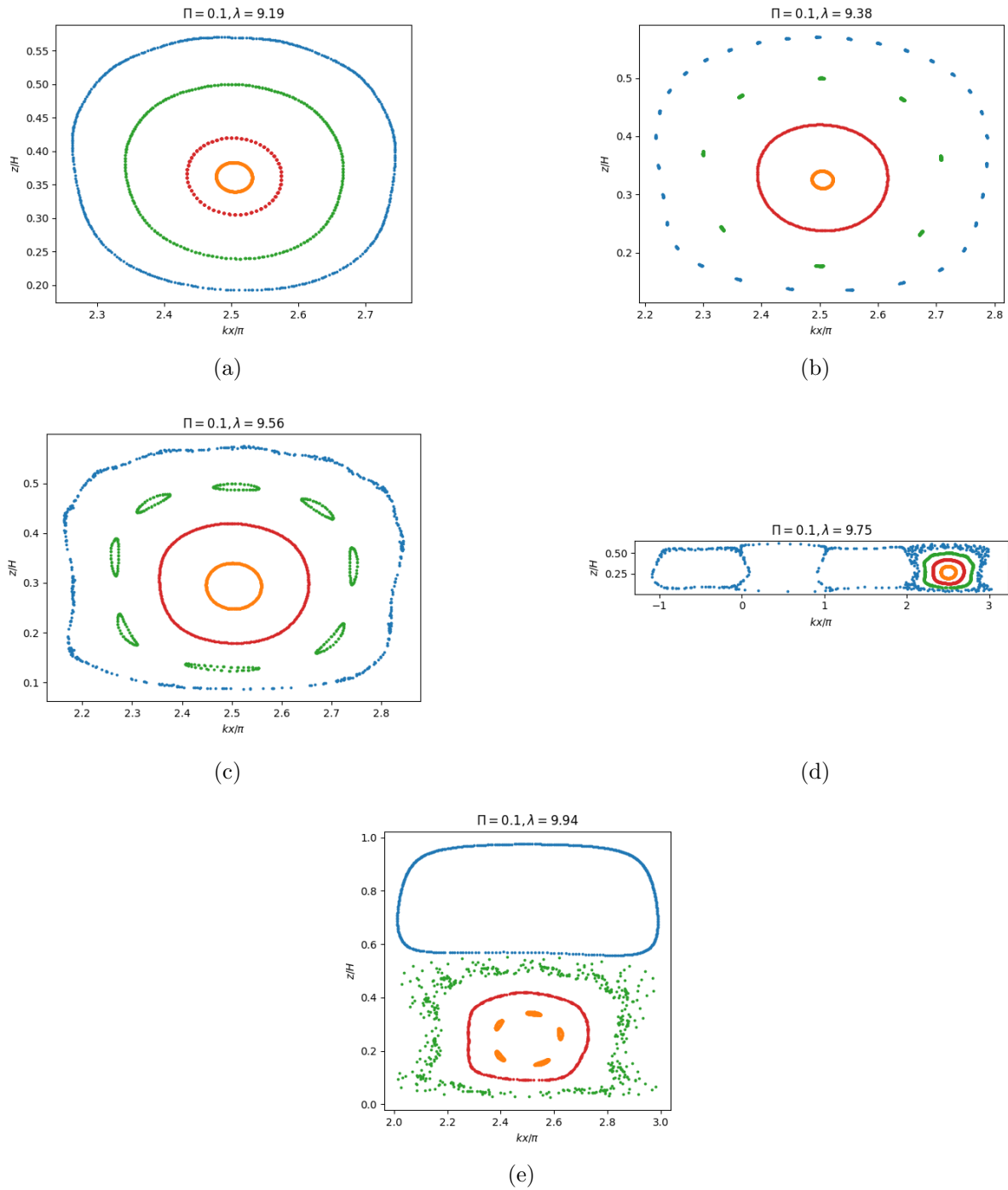
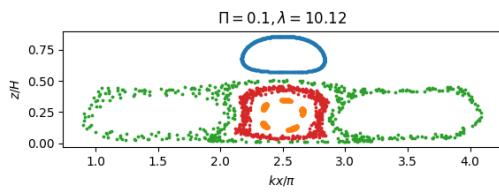
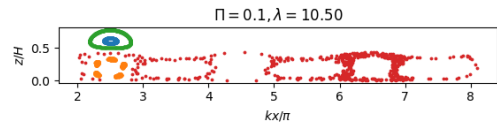


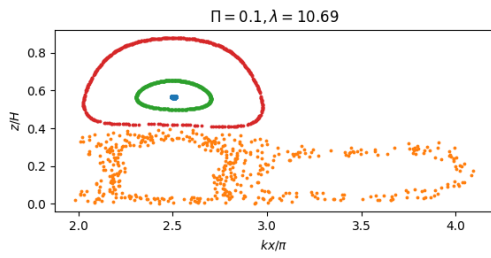
Figure 15: Tidal maps for constant  $\Pi = 0.1$ , and  $\lambda$  varying between 9.19 and 9.94.



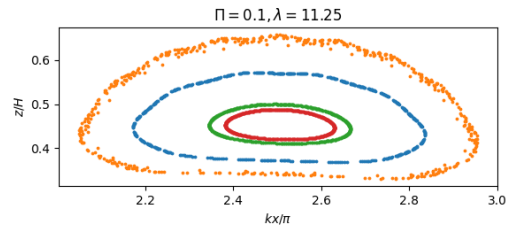
(a)



(b)



(c)



(d)

Figure 16: Tidal maps for constant  $\Pi = 0.1$ , and  $\lambda$  varying between 10.12 and 11.25.

### 5.3.2 Varying $\Pi$

The tidal maps from experiment "ZoomVar- $\Pi$ " are shown in figures (18) and (19). In the figure, we see eight different trajectories for constant  $\lambda = 10.14$  and  $\Pi$  varying between 0.05 and 0.104.

Figure (18a) shows the tidal map for  $\Pi = 0.050$  and  $\lambda = 10.14$ . The maps of the blue and green trajectories orbit around an elliptic point at  $z/H = 0.7$ ,  $kx/\pi = 2.5$ . The Fourier spectrum of the blue trajectory has a noise width of about 0.02, and that of the green trajectory of about 0.05. Although the green particle trajectory is therefore chaotic by our definition, its tidal map does not exhibit the confetti-like structure that accompanies chaotic advection. The maps of the red and orange trajectories orbit around an elliptic point at  $z/H = 0.02$ ,  $kx/\pi = 2.5$ , and the map of the red trajectory has small gaps. Both their Fourier spectra have a noise width of about 0.01.

Figure (18c) shows the tidal map for  $\Pi = 0.073$  and  $\lambda = 10.14$ . The maps of the blue and green trajectories orbit around an elliptic point at  $z/H = 0.7$ ,  $kx/\pi = 2.5$ . The Fourier spectrum of the blue trajectory has a noise width of about 0.02, and that of the green trajectory of about 0.01. The maps of the red and orange trajectories orbit around an elliptic point at  $z/H = 0.02$ ,  $kx/\pi = 2.5$ . Both their Fourier spectra have a noise width of about 0.01.

Figure (18b) shows the tidal map for  $\Pi = 0.081$  and  $\lambda = 10.14$ . The map of the blue trajectory orbits around an elliptic point at  $z/H = 0.7$ ,  $kx/\pi = 2.5$ . The Fourier spectrum of the blue trajectory has a noise width of about 0.01. The maps of the red and orange trajectories orbit around an elliptic point at  $z/H = 0.02$ ,  $kx/\pi = 2.5$ . Both their Fourier spectra have a noise width of about 0.01. The map of the green trajectory travels between sandwaves, and has a confetti-like structure. Its Fourier spectrum has noise width 0.06. This means that the green particle is in a region of chaotic advection.

Figure (18d) shows the tidal map for  $\Pi = 0.089$  and  $\lambda = 10.14$ . The map of the blue trajectory orbits around an elliptic point at  $z/H = 0.7$ ,  $kx/\pi = 2.5$ , and its Fourier spectrum has a noise width of about 0.02. The maps of the other trajectories orbit around an elliptic point at  $z/H = 0.25$ ,  $kx/\pi = 2.5$ . The map of the orange trajectory looks continuous, and its Fourier spectrum has a noise width of about 0.01. The map of the red trajectory jumps between eight islands, and its Fourier spectrum has a noise width of about 0.02. The map of the green orbit has a confetti-like structure, and its Fourier spectrum has a noise width of about 0.1. We see that the region of chaotic advection has increased in strength.

Figure (19a) shows the tidal map for  $\Pi = 0.097$  and  $\lambda = 10.14$ . The map of the blue trajectory orbits around an elliptic point at  $z/H = 0.7$ ,  $kx/\pi = 2.5$ , and its Fourier spectrum has a noise width of about 0.01. The maps of the red and orange trajectories orbit around an elliptic point at  $z/H = 0.25$ ,  $kx/\pi = 2.5$ , and have a confetti-like structure. The Fourier spectrum of the red trajectory has a noise width of about 0.08, and that of the orange trajectory has a noise width of about 0.02. The map of the green orbit

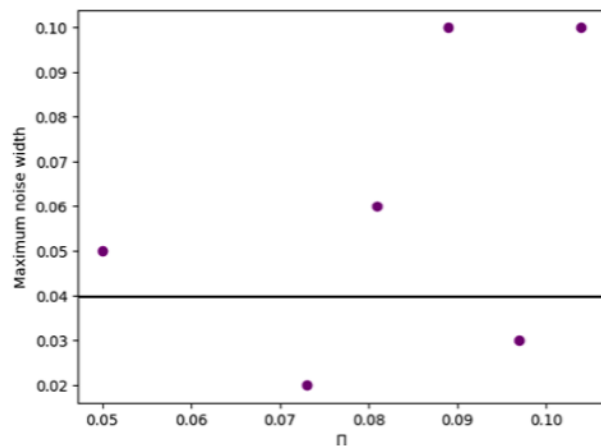


Figure 17: Maximum noise width (vertical axis) as a function of  $\Pi$  (horizontal axis). The black horizontal line at noise width 0.04 denotes the noise width above which trajectories are considered chaotic.

jumps between four sand waves to the right of its initial position, and its Fourier spectrum has a noise width of about 0.03. The region of chaotic advection seems to have disappeared.

Figure (19b) shows the tidal map for  $\Pi = 0.104$  and  $\lambda = 10.14$ . The map of the blue trajectory orbits around an elliptic point at  $z/H = 0.7$ ,  $kx/\pi = 2.5$ , and its Fourier spectrum has a noise width of about 0.02. The maps of the red and orange trajectories orbit around an elliptic point at  $z/H = 0.25$ ,  $kx/\pi = 2.5$ , and have a confetti-like structure. The Fourier spectrum of the red trajectory has a noise width of about 0.1, and that of the orange trajectory has a noise width of about 0.01. The map of the green orbit jumps between four sand waves to the left of its initial position, and its Fourier spectrum has a noise width of about 0.04.

In figures (18a) and (18c), we see very little qualitative change in the tidal maps of the particles, while  $\Pi$  increases from 0.05 to 0.073. However, once  $\Pi = 0.081$ , we suddenly see islands and mixing regions. This suggests that the occurrence of stirring by chaotic advection is very sensitive to the value of  $\Pi$ . We can also see in figure (19a) that the green particle skews to the sand waves on the right for parameter values  $\lambda = 10.14$ ,  $\Pi = 0.967$ , figure (11c) shows that the green particle is contained for parameter values  $\lambda = 10.14$ ,  $\Pi = 0.1$ , and figure (19b) shows that the green particle skews to the sand waves on the left for parameter values  $\lambda = 10.14$ ,  $\Pi = 0.104$ . This suggests that  $\Pi$  is responsible for determining the direction of travel for particles.

Figure (17) shows the maximum noise width as a function of  $\Pi$ , where the black line denotes the chaos threshold. We see that the noise width varies wildly for consecutive values of  $\Pi$ . This means that the shape and strength of the region of chaotic advection is very sensitive to the height of the sand waves.

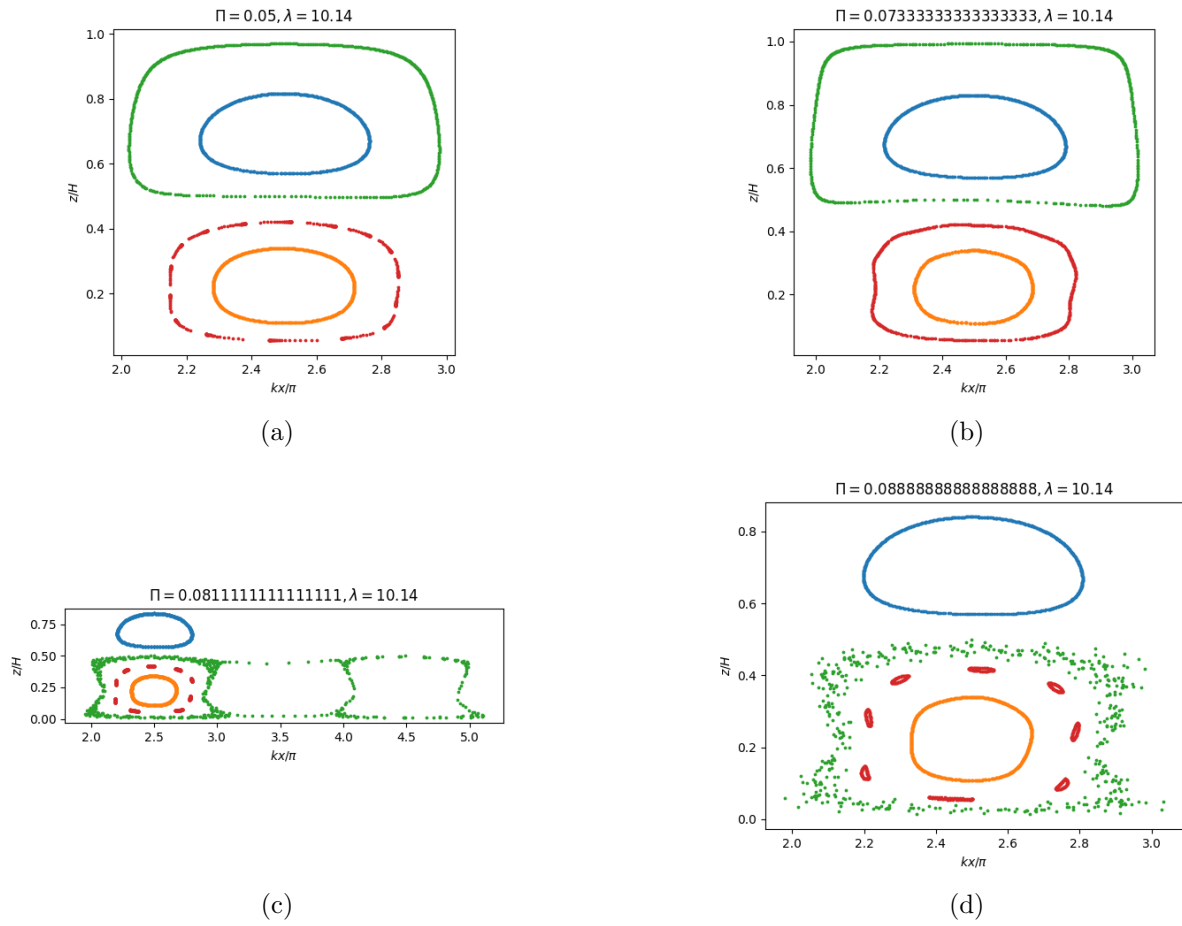
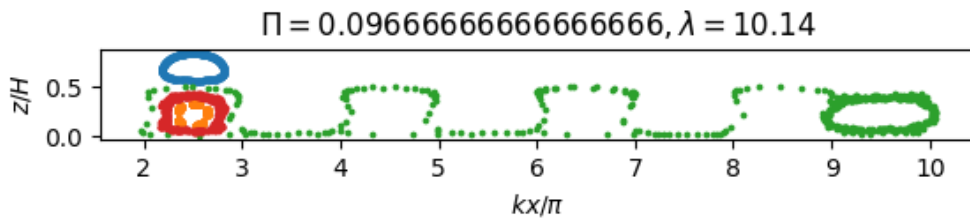
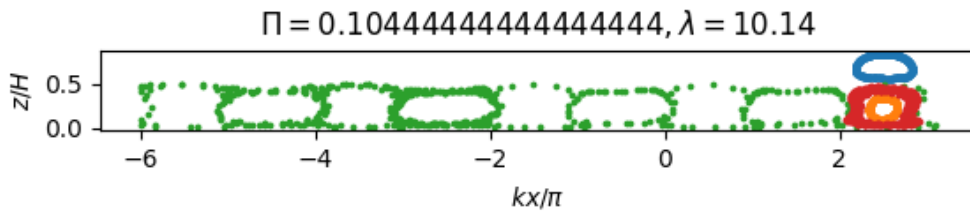


Figure 18: Tidal maps with constant  $\lambda = 15.00$  and varying  $\Pi$  between 0.05 and 0.09.



(a)



(b)

Figure 19: Tidal maps with constant  $\lambda = 15.00$  and varying  $\Pi$  between 0.097 and 0.104.



## 6 Discussion

Our experiment "Default" was aimed at our first research goal of exploring particle behaviour in a realistic environmental setting. We did this by simulating the conditions typically found in the North Sea. Under these circumstances, we have found some interesting results. First of all, we have found that the initial depth of a particle is of great importance to its trajectory. While tidal maps of particles above roughly  $z/H = 0.5$  remain captured around elliptical points, tidal maps of particles below roughly  $z/H = 0.5$  freely travel between sand waves. A remarkable result is that, according to our definition of chaotic advection, stirring by chaotic advection occurs in this default case, both above and below  $z/H = 0.5$ . Although noise width is not the best measure of chaos, it is certain that, for some initial conditions in this system, the particle trajectories are neither periodic nor quasi-periodic, and seem chaotic. Particles trace confetti-like trajectories in phase-space, and move seemingly randomly. We have also seen that, after traveling erratically for a while, a particle may be captured by some elliptic point at a different sand wave than where it was released. This means that tidal currents play a significant role in the transport of particles on a small scale ( $O(1 \text{ km})$ ). The second set of experiments, "SearchVar- $\lambda$ " and "SearchVar-II", has shown multiple regions of chaotic advection. We have seen a trend where the noise width generally increases with  $\Pi$ , but this is not the case for  $\lambda$ . This means that the height of sand waves can be seen as an indicator of the strength of chaotic advection if it occurs, and then the sand wave length has some very specific values for which chaotic advection can take place.

The behaviour of particle trajectories for parameter values near those that exhibit regions of chaotic advection is studied in the third set of experiments, "ZoomVar- $\lambda$ " and "ZoomVar-II". We see in figure (15b) that the tidal maps, which were smooth lines in (15a), have contracted into points. These points become small islands in (15c). These points and islands are also found in other studies of two-dimensional non-integrable Hamiltonian systems, such as in (Beerens et al. 1994, ch. 3, fig. 3). Beerens et al. relate these islands with the bifurcation of elliptic points; at certain parameter values, elliptic points split, yielding more elliptic points. With enough bifurcations, *mixing regions* originate. These are regions where chaotic stirring occurs, so that particle trajectories seem erratic. The green particle in figure (15e) is in such a mixing region; its tidal map has an erratic confetti-like structure, and its Fourier spectrum has a high noise width of 0.08. Remarkable, this same bifurcation is not observed in experiment "ZoomVar-II", when we approach the region of chaotic advection from lower values of  $\Pi$ . This might be caused by a too large step size for  $\Pi$ , but it might also mean that the occurrence of chaotic advection is caused by the sand wave length value, while the sand wave height determines the strength of this chaotic advection as discussed before.

These findings indicate that tidal currents play a significant role in the transport of passive particles in shallow tidal areas. This result was also found by previous studies, such as (Ridderinkhof and Zimmerman 1992). It is important to note the scale of this transport, though; as we have seen, passive particles may travel between sand waves, but only a small number of sand waves. Increasing the number of tidal periods in the simulation does not seem to affect this number. This means that this transport of particles will not be detectable on a scale much larger than those of the sand waves ( $O(1 \text{ km})$ ). In fact, Sterl et al. 2020 have shown that tidal currents can be neglected in calculations of the global transport of particles in the open seas. Depending on the desired precision and resolution of future models that want to calculate the trajectories of passive particles in a system that contains shallow tidal areas, extra care must be taken to account for stirring by chaotic advection in those areas.

## 6.1 Model limitations

As discussed in the introduction, this study makes use of a simple model. This means that we have made many approximations in order to be able to analyze the system easier. But as the results show, the system is very sensitive to initial conditions. The combination of those two factors makes this model unfit to make any quantitative predictions. Also, the simplification of the bottom topography might be a significant source of error; we assume the sand waves to be perfectly sinusoidal, while real sand waves do not look like this at all (see figure 1).

Also, the method used to quantify chaos is a bit hand-wavy. There is no clear distinction between stirring by chaotic advection and other non-periodic behaviour. This means that the analysis of chaotic advection can not be very thorough.

The used second order integration method, Störmer-Verlet, generally performs much better than its formal order suggests. However, as mentioned in (3.1), its precision is dependent on the step size  $h$ . Because any simulation necessarily must finish in a finite amount of time, this step-size must be non-zero, and therefore the numerical integration can not determine the position of a particle precisely. In regions of chaotic stirring, where the slightest deviation in particle position means a wildly different trajectory, this limitation means that it is near impossible to predict particle positions in these regions.

## 6.2 Future research

This simple research has shown very interesting results, and it might be very interesting to continue research in this area. A simple thing that can be done is to use Lyapunov-exponents as a measure of chaos (Wilkinson 2017). Lyapunov-exponents are a measure for how fast particles that are 'near' each other diverge in a flow.

We have also seen that particles can travel between sand waves if their trajectories are chaotic enough. An interesting observation that has not been studied in this research is that this sand wave traveling increases when either  $\lambda$  or  $\Pi$  increases. Figure (20) shows that, for  $\lambda = 20$  and  $\Pi = 0.1$ , the red particle travels between ten sand waves. This is a significantly higher number of sand waves than in any of the systems that we have seen in this study. The relation between sand wave length, sand wave height and the number of traveled sand waves for particles in the flow may be worthwhile to investigate.

Another interesting topic of research is to take more details into account, in order to make a more accurate model. This could for instance mean that measurements of bottom topography can be taken into account, or that more tidal constituents contribute to the flow field.

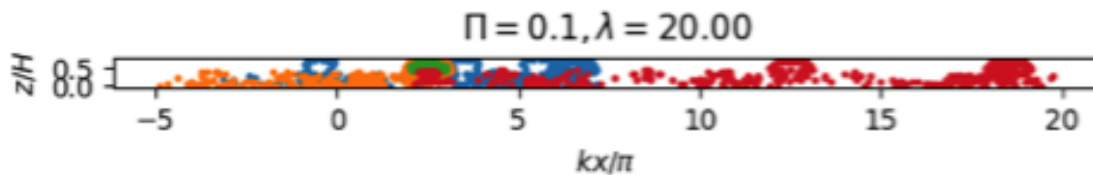


Figure 20: Tidal map in a system where  $\lambda = 20$  and  $\Pi = 0.1$ . we see that the red particle travels between ten different sand waves, and the orange particle travels between four.

## 7 Conclusions

We see that the presented method, when applied on a default environmental setting resembling conditions in the North Sea, gives rise to chaotic particle trajectories. Particles below roughly  $z/H = 0.5$  may travel erratically between different sand waves, and particles may even become trapped above a different sand wave than where they were released. Particles above roughly  $z/H = 0.5$  are confined above a sand wave, but may still show confetti-like tidal maps. This means that stirring may occur in these regions as well.

We have also found other regions where stirring by chaotic advection occurs. If we increase  $\Pi$  while keeping  $\lambda$  constant, there is a clear trend that a larger value of  $\Pi$  gives rise to more stirring by chaotic advection. There is however no such trend apparent when increasing  $\lambda$  while keeping  $\Pi$  constant; there are specific values of  $\lambda$  for which stirring by chaotic advection occurs, while there is no global relation between  $\lambda$  and noise width detectable. This means that sand wave height may play a more significant role in causing chaotic advection than sand wave length.

Varying  $\lambda$  or  $\Pi$  near regions of chaotic stirring gives rise to elliptic point bifurcation. Bifurcated elliptic points are visible in tidal maps as 'islands' around which the particles orbit. If we approach a region of chaotic advection, these islands keep splitting into more islands, until particle trajectories become chaotic.

# Appendices

## A Perturbed state velocity field

The velocity field of the perturbed state are described by equations 2.14a and 2.14b. It follows from the definition of  $\Psi$  that  $\hat{\Psi}_{-n}^* = \hat{\Psi}_n$  if  $n$  is odd, and  $\hat{\Psi}_{-n}^* = -\hat{\Psi}_n$  if  $n$  is even (here,  $\hat{\Psi}_n^*$  denotes the complex conjugate of  $\hat{\Psi}_n$ ). These relations allow us to further elaborate on the velocity components;

$$\begin{aligned} \tilde{u}(x, z, t) &= \Pi \left( \left[ \frac{d\hat{\Psi}_0(z, t)}{dz} e^{ikx} + c.c. \right] + \sum_{n=1}^{\infty} \left[ \left( \frac{d\hat{\Psi}_n(z, t)}{dz} e^{in\sigma t} + \frac{d\hat{\Psi}_{-n}(z, t)}{dz} e^{-in\sigma t} \right) e^{ikx} + c.c. \right] \right), \\ \tilde{w}(x, z, t) &= k\Pi \left( \left[ -i\hat{\Psi}_0(z, t) e^{ikx} + c.c. \right] + \sum_{n=1}^{\infty} \left[ \left( -i\hat{\Psi}_n(z, t) e^{in\sigma t} - i\hat{\Psi}_{-n}(z, t) e^{-in\sigma t} \right) e^{ikx} + c.c. \right] \right). \end{aligned}$$

Expanding  $e^{ikx}$  and  $e^{-ikx}$  in their real and imaginary components:

$$\begin{aligned} \tilde{u}(x, z, t) &= 2\Pi \left[ i \frac{d\hat{\Psi}_0(z, t)}{dz} \sin(kx) \right] \\ &\quad + 2\Pi \sum_{\text{positive odd } n} \left[ \frac{d\hat{\Psi}_n(z, t)}{dz} e^{in\sigma t} + c.c. \right] \cos(kx) \\ &\quad + 2\Pi \sum_{\text{positive even } n} \left[ i \frac{d\hat{\Psi}_n(z, t)}{dz} e^{in\sigma t} + c.c. \right] \sin(kx), \\ \tilde{w}(x, z, t) &= -2k\Pi \left[ i\hat{\Psi}_0(z, t) \cos(kx) \right] \\ &\quad + 2k\Pi \sum_{\text{positive odd } n} \left[ \hat{\Psi}_n(z, t) e^{in\sigma t} + c.c. \right] \sin(kx) \\ &\quad - 2k\Pi \sum_{\text{positive even } n} \left[ i\hat{\Psi}_n(z, t) e^{in\sigma t} + c.c. \right] \cos(kx). \end{aligned}$$

We will now use the parameter scalings 2.15a, 2.15b and 2.15c introduced in chapter 2. Hereafter we shall omit primes, with the understanding that we mean the dimensionless variables.

Substituting the dimensionless variables we obtain:

$$\begin{aligned}
\tilde{u}(x, z, t) &= 2\Pi \left[ i \frac{d\hat{\Psi}_0(z, t)}{dz} \sin(x) \right] \\
&+ 2\Pi \sum_{\text{positive odd } n} \left[ \frac{d\hat{\Psi}_n(z, t)}{dz} e^{int} + c.c. \right] \cos(x) \\
&+ 2\Pi \sum_{\text{positive even } n} \left[ i \frac{d\hat{\Psi}_n(z, t)}{dz} e^{int} + c.c. \right] \sin(x), \\
\tilde{w}(x, z, t) &= -2\Pi \left[ i\hat{\Psi}_0(z, t) \cos(x) \right] \\
&+ 2\Pi \sum_{\text{positive odd } n} \left[ \hat{\Psi}_n(z, t) e^{int} + c.c. \right] \sin(x) \\
&- 2\Pi \sum_{\text{positive even } n} \left[ i\hat{\Psi}_n(z, t) e^{int} + c.c. \right] \cos(x).
\end{aligned}$$

Expanding the complex conjugates:

$$\begin{aligned}
\tilde{u}(x, z, t) &= 4\Pi \left[ -\frac{1}{2} \frac{d}{dz} \text{Im}(\hat{\Psi}_0(z, t)) \sin(x) \right] \\
&+ 4\Pi \sum_{\text{positive odd } n} \left[ \frac{d}{dz} \text{Re}(\hat{\Psi}_n(z, t)) \cos(nt) - \frac{d}{dz} \text{Im}(\hat{\Psi}_n(z, t)) \sin(nt) \right] \cos(x) \\
&+ 4\Pi \sum_{\text{positive even } n} \left[ \frac{d}{dz} \text{Re}(\hat{\Psi}_n(z, t)) \sin(nt) - \frac{d}{dz} \text{Im}(\hat{\Psi}_n(z, t)) \cos(nt) \right] \sin(x), \\
\tilde{w}(x, z, t) &= -4\Pi \left[ \frac{1}{2} \text{Im}(\hat{\Psi}_0(z, t)) \cos(x) \right] \\
&+ 4\Pi \sum_{\text{positive odd } n} \left[ \text{Re}(\hat{\Psi}_n(z, t)) \cos(nt) - \text{Im}(\hat{\Psi}_n(z, t)) \sin(nt) \right] \sin(x) \\
&- 4\Pi \sum_{\text{positive even } n} \left[ \text{Re}(\hat{\Psi}_n(z, t)) \sin(nt) - \text{Im}(\hat{\Psi}_n(z, t)) \cos(nt) \right] \cos(x).
\end{aligned}$$

## B Symplectic method

### B.1 Hamiltonian of the system

As we saw in chapter (2), our system is Hamiltonian. In particular,

$$\psi(x, z, t) = \tilde{\psi}(x, z, t) + \psi_b(x, z, t), \quad (\text{B.1})$$

where  $\psi$  is the Hamiltonian of the system,  $\tilde{\psi}$  is the Hamiltonian of the perturbed state and  $\psi_b$  is the Hamiltonian of the basic state. Now, we define canonical coordinates  $p = x$ ,  $q = z$  and  $t = t$ . Then, requiring that

$$\frac{dp}{dt} = -\frac{\partial\psi}{\partial q}, \quad \frac{dq}{dt} = \frac{\partial\psi}{\partial p}, \quad (\text{B.2a})$$

it follows from (2.20) (if we cut after the second harmonic component of  $\tilde{u}$  and  $\tilde{w}$ ) that

$$\begin{aligned} \psi(p, q, t) &= 2\lambda\Pi \operatorname{Im}(\Psi_0(q)) \sin(p) \\ &\quad - 4\lambda\Pi \operatorname{Re}(\Psi_1(q)) \cos(p) \cos(t) \\ &\quad + 4\lambda\Pi \operatorname{Im}(\Psi_1(q)) \cos(p) \sin(t) \\ &\quad - 4\lambda\Pi \operatorname{Re}(\Psi_2(q)) \sin(p) \sin(2t) \\ &\quad + 4\lambda\Pi \operatorname{Im}(\Psi_2(q)) \sin(p) \cos(2t) \\ &\quad + \frac{\lambda}{2} \left( -\frac{1}{3}q^3 + q^2 + z_c(2 + z_c)q \right) \cos(t). \end{aligned} \quad (\text{B.3})$$

### B.2 Splitting methods

As laid out in chapter (2), a symplectic map is a map that preserves volumes in phase space. A key insight is the fact that the composition of two symplectic maps is again symplectic. This means that we can split the Hamiltonian, and construct symplectic maps for all resulting pieces. If we then compose all the pieces after each other, the resulting map is again symplectic. In our case, it is natural to consider the following splitting:

$$\begin{aligned} \psi(p, q, t) &= H_0(p, q) \\ &\quad + H_1(p, q) \cos(t) \\ &\quad + H_2(p, q) \sin(t) \\ &\quad + H_3(p, q) \sin(2t) \\ &\quad + H_4(p, q) \cos(2t) \\ &\quad + H_5(p, q) \cos(t), \end{aligned} \quad (\text{B.4})$$

where

$$H_0(p, q) = 2\lambda\Pi \operatorname{Im}(\Psi_0(q)) \sin(p), \quad (\text{B.5})$$

$$H_1(p, q) = -4\lambda\Pi \operatorname{Re}(\Psi_1(q)) \cos(p), \quad (\text{B.6})$$

$$H_2(p, q) = 4\lambda\Pi \operatorname{Im}(\Psi_1(q)) \cos(p), \quad (\text{B.7})$$

$$H_3(p, q) = -4\lambda\Pi \operatorname{Re}(\Psi_2(q)) \sin(p), \quad (\text{B.8})$$

$$H_4(p, q) = 4\lambda\Pi \operatorname{Im}(\Psi_2(q)) \sin(p), \quad (\text{B.9})$$

$$H_5(p, q) = \frac{\lambda}{2} \left( -\frac{1}{3}q^3 + q^2 + z_c(2 + z_c)q \right), \quad (\text{B.10})$$

where we consider each of the lines in equation (B.4) as a separate Hamiltonian, and determine a symplectic map for each of them. If we then compose them, we obtain a symplectic map for the total system.

### B.3 Non-autonomous systems

A lot of the Hamiltonian components of (B.4) depend explicitly on time. Systems that are described by such Hamiltonians are called non-autonomous. However, since autonomous systems are generally easier to deal with, we would like to find some coordinate transformation such that we may consider the system to be autonomous. We have seen in section (??) that we can add time as a dependent variable, in order to make a system autonomous. In this case we can achieve this using a local time transformation.

Note that the non-autonomous Hamiltonian components in (B.4) are of the form

$$\begin{aligned} H_i(p, q, t) &= f(p, q) \sin(nt), \text{ or} \\ H_i(p, q, t) &= f(p, q) \cos(nt), \end{aligned}$$

for some function  $f$  and some  $n$ . We will look at the case where  $H_i(p, q, t) = f(p, q) \sin(nt)$ , but the case where  $H_i(p, q, t) = f(p, q) \cos(nt)$  is completely similar.

We want to find a local time transformation  $\tau$  that makes our system autonomous. We can do this by requiring that

$$\frac{dt}{d\tau} = \frac{1}{\sin(nt)}, \quad (\text{B.11})$$

so that

$$\frac{dp}{d\tau} = \frac{dt}{d\tau} \frac{dp}{dt} = -\frac{\partial f(p, q)}{\partial q}, \quad (\text{B.12})$$

$$\frac{dq}{d\tau} = \frac{dt}{d\tau} \frac{dq}{dt} = \frac{\partial f(p, q)}{\partial p}. \quad (\text{B.13})$$

This means that  $\frac{d\tau}{dt} = \sin(nt)$ , so that  $\tau = -\frac{1}{n} \cos(nt)$ .

### B.4 Component symplectic maps

As mentioned in section (??), our goal now is to find coordinate transformations such that the component Hamiltonians  $H_i$  are of the form  $H_i(p, q) = F_i(p) + G_i(q)$ , for some functions  $F_i, G_i$ . Note that  $H_5$  is already in this form, and that the components  $H_i, 0 \leq i \leq 4$  are of either of the forms

$$\begin{aligned} H_i(p, q) &= f_i(q) \sin(p), \text{ or} \\ H_i(p, q) &= f_i(q) \cos(p), \end{aligned}$$

for some function  $f_i$ . Again, the procedure is completely similar for both of these cases, so we will only look at the first case where  $H_i(p, q) = f_i(q) \sin(p)$ .

Suppose we have a system described by the Hamiltonian  $H_i(p, q) = f_i(q) \sin(p)$ . We then have Hamilton's canonical equations of motion

$$\frac{dp}{dt} = -\frac{\partial H_i}{\partial q} = -f'_i(q) \sin(p), \quad \frac{dq}{dt} = \frac{\partial H_i}{\partial p} = f_i(q) \cos(p). \quad (\text{B.14})$$

A key insight is the fact that  $\frac{d^2q}{dt^2}$  does not depend on  $p$ :

$$\frac{d^2q}{dt^2} = \frac{dq}{dt} \frac{d}{dq} f_i(q) \cos(p) + f_i(q) \frac{dp}{dt} \frac{d}{dp} \cos(p) \quad (\text{B.15})$$

$$= f_i(q) f'_i(q) \cos^2(p) + f_i(q) f'_i(q) \sin^2(p) \quad (\text{B.16})$$

$$= f_i(q) f'_i(q). \quad (\text{B.17})$$

Now let  $v = \frac{dq}{dt}$ , and consider a new Hamiltonian  $H_i^*(q, v) = \frac{f_i(q)^2}{2} + \frac{v^2}{2}$ . Note that this Hamiltonian is of the required form  $H_i^*(q, v) = F_i^*(q) G_i^*(v)$  for the Störmer-Verlet method. Hamilton's canonical equations of motion now read

$$\frac{dq}{dt} = v, \quad (\text{B.18})$$

$$\frac{dv}{dt} = f_i(q) f'_i(q). \quad (\text{B.19})$$

Using Störmer-Verlet and the values of  $q(t)$  and  $v(t)$  at time  $t$  we obtain an approximation of the values of  $q(t+h)$  and  $v(t+h)$  after a timestep  $h$ . We retrieve the coordinate  $p(t+h)$  by requiring that

$$p(t+h) = \cos^{-1} \left( \frac{v(t+h)}{f_i(q(t+h))} \right). \quad (\text{B.20})$$

One may now object that it might be impossible to obtain the correct value for  $p(t+h)$ , since the cosine is a non-injective function. However, if we consider the 'branches' of the cosine (i.e. the intervals  $[a, b] \in \mathbb{R}$  such that  $\cos : [a, b] \rightarrow [-1, 1], x \mapsto \cos(x)$  is a bijection), it turns out that the value of  $p$  will never leave its 'branch'. Therefore it is sufficient to know  $p(t)$  in order to uniquely determine  $p(t+h)$  from the values of  $q(t+h)$  and  $v(t+h)$ . We can therefore obtain an approximation for  $p(t+h)$  and  $q(t+h)$  using a symplectic map.

## B.5 Composition of symplectic maps

Using the time transformations and the method described above we can determine symplectic step relations  $p_i : p(t) \mapsto p(t+h)$  and  $q_i : q(t) \mapsto q(t+h)$  for all of the component Hamiltonians  $H_i$ . The composition of these step relations is obtained by simply performing them after each other at time  $t$  (so, while we perform certain step relations before others, we consider them to be simultaneous in time). This composition is trivially symplectic.



## C Additional results

### C.1 Regions of chaotic advection - vary $\Pi$

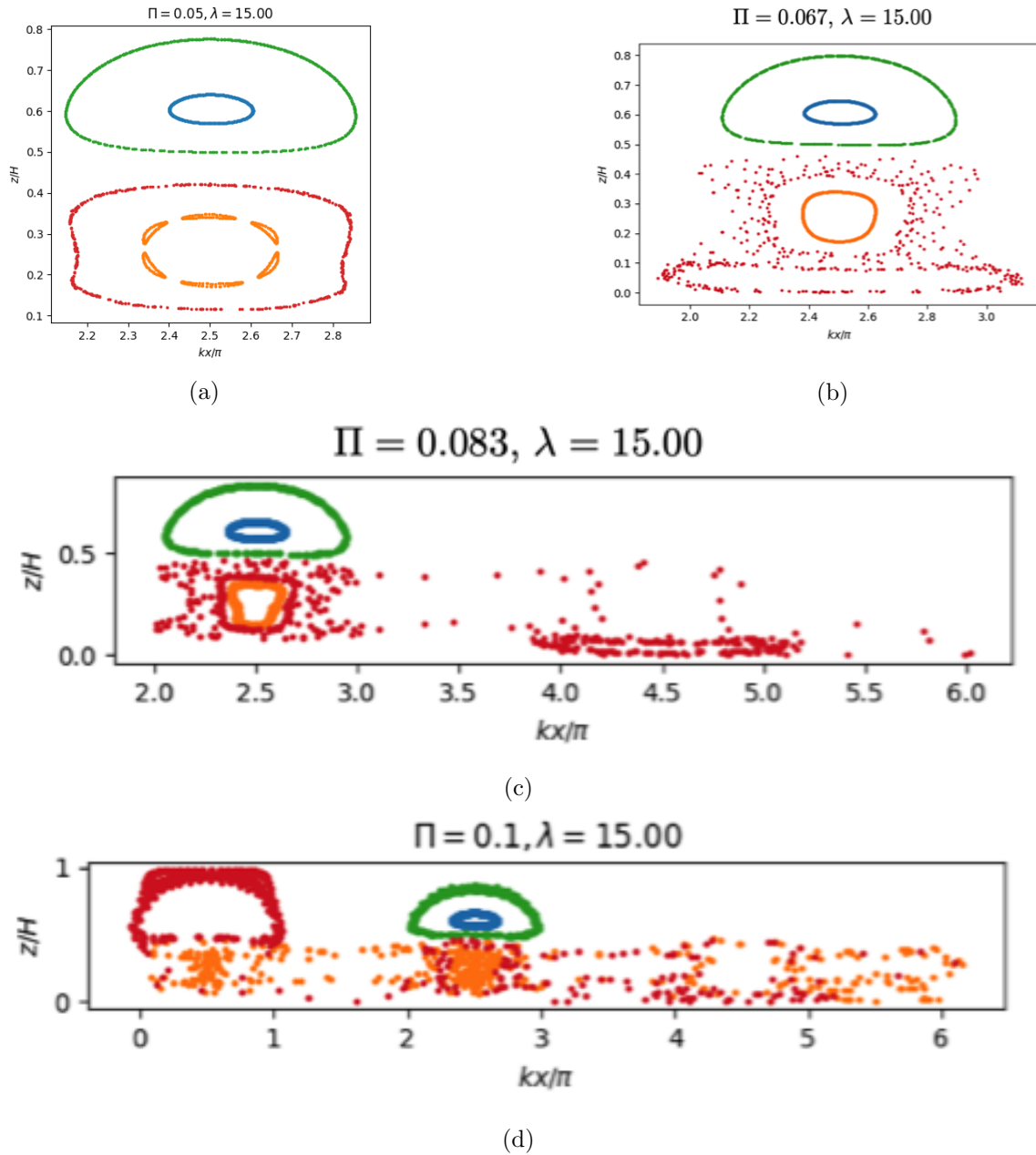


Figure 21: Tidal maps for constant  $\lambda = 15.00$ , and for varying  $\Pi$  between 0.05 and 0.1

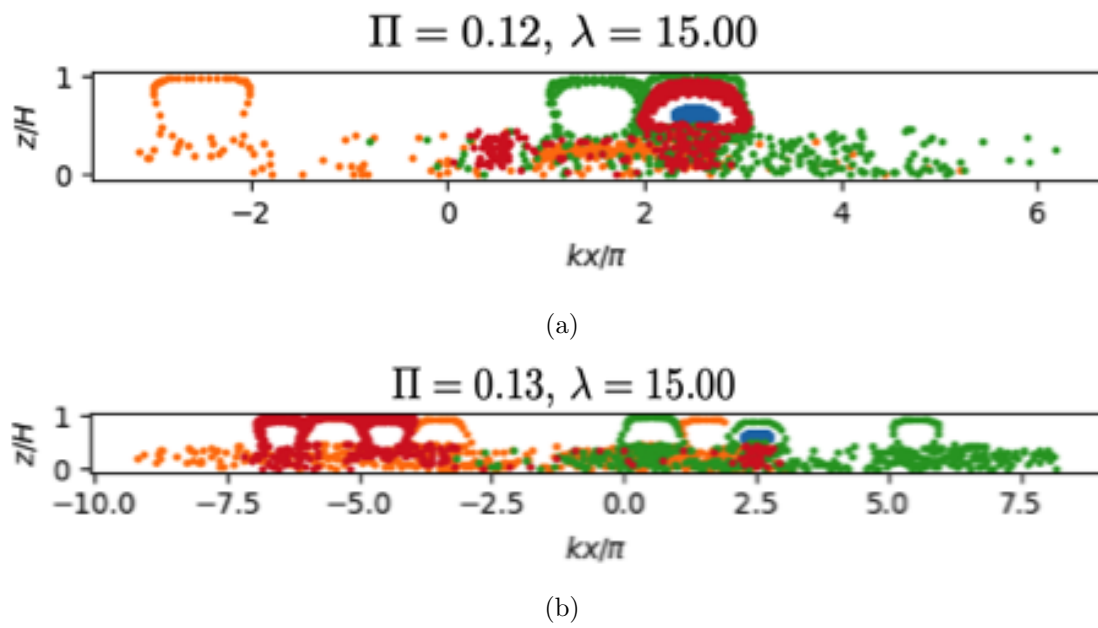


Figure 22: Tidal maps for constant  $\lambda = 15.00$ , and for varying  $\Pi$  between 0.1 and 0.133

## References

- Abdullaev, S. (1999). “A new integration method of Hamiltonian systems by symplectic maps”. In: *Journal of Physics A General Physics* 32, pp. 2745–2766. DOI: 10.1088/0305-4470/32/15/004.
- Aref, H. (1984). “Stirring by chaotic advection”. In: *Journal of Fluid Mechanics* 143, pp. 1–21. DOI: 10.1017/S0022112084001233.
- Berens, S.P., H. Ridderinkhof, and J.T.F. Zimmerman (1994). “An analytical study of chaotic stirring in tidal areas”. In: *Chaos, Solitons and Fractals* 4.6. Special Issue: Chaos Applied to Fluid Mixing, pp. 1011–1029. ISSN: 0960-0779. DOI: [https://doi.org/10.1016/0960-0779\(94\)90136-8](https://doi.org/10.1016/0960-0779(94)90136-8). URL: <https://www.sciencedirect.com/science/article/pii/0960077994901368>.
- Besio, G., P. Blondeaux, M. Brocchini, and G. Vittori (2004). “On the modeling of sand wave migration”. In: *Journal of Geophysical Research* 109.
- Boucher, J. and D. Friot (2017). *Primary microplastics in the oceans: a global evaluation of sources*. Ed. by J.M. de Sousa C.G. Lundin. IUCN, Gland, Switzerland. ISBN: 978-2-8317-1827-9.
- Campmans, G.H.P. (2018). “Modeling storm effects on sand wave dynamics”. In: *University of Twente PhD Thesis*, Chapter 1. DOI: 10.3990/1.9789036546003.
- Dalrymple, R.W. and K. Choi (2003). *Sediment transport by tides*. Ed. by G.V. Middleton, M.J. Church, M. Coniglio, L.A. Hardie, and F.J. Longstaffe. Dordrecht: Springer Netherlands, pp. 606–609. ISBN: 978-1-4020-3609-5. DOI: 10.1007/978-1-4020-3609-5\_181. URL: [https://doi.org/10.1007/978-1-4020-3609-5\\_181](https://doi.org/10.1007/978-1-4020-3609-5_181).
- Gerkema, T. (2000). “A linear stability analysis of tidally generated sand waves”. In: *Journal of Fluid Mechanics* 417, pp. 303–322.
- Hairer, E., C. Lubich, and G. Wanner (2003). “Geometric numerical integration illustrated by the Stormer-Verlet method”. In: *Acta Numerica* 12, pp. 399–450. DOI: 10.1017/S0962492902000144.
- (2006). *Geometric Numerical Integration - structure-preserving algorithms for ordinary differential equations*. Ed. by R. Bank, R.L. Graham, J. Stoer, R. Varga, and H. Yserentant. 2nd. Springer. ISBN: 3-540-30663-3.
- Muller, Meinard (2015). “The Fourier Transform in a Nutshell”. In: pp. 39–57. ISBN: 978-3-319-21944-8.
- Ottino, J.M. (1990). “Mixing, Chaotic Advection, and Turbulence”. In: *Annual Review of Fluid Mechanics* 22.1, pp. 207–254. DOI: 10.1146/annurev.fl.22.010190.001231. eprint: <https://doi.org/10.1146/annurev.fl.22.010190.001231>. URL: <https://doi.org/10.1146/annurev.fl.22.010190.001231>.
- Ridderinkhof, H. and J.T.F. Zimmerman (1992). “Chaotic Stirring in a Tidal System”. In: *Science* 258.5085, pp. 1107–1111. ISSN: 00368075, 10959203. URL: <http://www.jstor.org/stable/2880508>.
- Sterl, M.F., P. Delandmeter, and E. van Sebille (2020). “Influence of Barotropic Tidal Currents on Transport and Accumulation of Floating Microplastics in the Global Open Ocean”. In: *Journal of Geophysical Research: Oceans* 125.2. e2019JC015583 10.1029/2019JC015583, e2019JC015583. DOI: <https://doi.org/10.1029/2019JC015583>. eprint: <https://agupubs.onlinelibrary.wiley.com/doi/pdf/10.1029/2019JC015583>. URL: <https://agupubs.onlinelibrary.wiley.com/doi/abs/10.1029/2019JC015583>.
- Tabor, M. (1989). *Chaos and Integrability in Nonlinear Dynamics: An Introduction*. 1st. Wiley-Interscience. ISBN: 0471827282.
- Wilkinson, Amie (2017). “What are Lyapunov exponents, and why are they interesting?” In: *Bull. Amer. Math. Soc.* 54.1, pp. 79–105.
- Zimmerman, J.T.F. (1976). “Mixing and flushing of tidal embayments in the Western Dutch Wadden Sea, part II: Analysis of mixing processes”. In: *Netherlands Journal of Sea Research* 10.4, pp. 397–

---

439. ISSN: 0077-7579. DOI: [https://doi.org/10.1016/0077-7579\(76\)90019-3](https://doi.org/10.1016/0077-7579(76)90019-3). URL: <https://www.sciencedirect.com/science/article/pii/0077757976900193>.